JOURNAL OF PETROLOGY | VOLUME 47 | NUMBER 2 | PAGES 329–353 | 2006 | doi:10.1093/petrology/egi077

Zircon Crystal Morphology, Trace Element Signatures and Hf Isotope Composition as a Tool for Petrogenetic Modelling: Examples From Eastern Australian Granitoids

E. A. BELOUSOVA[1]*, W. L. GRIFFIN[1,2] AND SUZANNE Y. O'REILLY[1]

[1]GEMOC ARC NATIONAL KEY CENTRE, DEPARTMENT OF EARTH AND PLANETARY SCIENCES, MACQUARIE UNIVERSITY, SYDNEY, NSW 2109, AUSTRALIA

[2]CSIRO EXPLORATION AND MINING, NORTH RYDE, NSW 2113, AUSTRALIA

RECEIVED MAY 13, 2004; ACCEPTED SEPTEMBER 19, 2005
ADVANCE ACCESS PUBLICATION OCTOBER 26, 2005

In situ *laser ablation inductively coupled plasma mass spectrometry analysis of trace elements, U–Pb ages and Hf isotopic compositions of magmatic zircon from I- and S-type granitoids from the Lachlan Fold Belt (Berridale adamellite and Kosciusko tonalite) and New England Fold Belt (Dundee rhyodacite ignimbrite), Eastern Australia, is combined with detailed studies of crystal morphology to model petrogenetic processes. The presented examples demonstrate that changes in zircon morphology, within single grains and between populations, generally correlate with changes in trace element and Hf-isotope signatures, reflecting the mixing of magmas and changes in the composition of the magma through mingling processes and progressive crystallization. The zircon data show that the I-type Kosciusko tonalite was derived from a single source of crustal origin, whereas the S-type Berridale adamellite had two distinct sources including a significant I-type magma contribution. Complex morphology and Hf isotope variations in zircon grains indicate a moderate contribution from a crustal component in the genesis of the I-type Dundee rhyodacite. The integration of data on morphology, trace elements and Hf isotope variations in zircon populations provides a tool for the detailed analysis of the evolution of individual igneous rocks; it offers new insights into the contributions of different source rocks and the importance of magma mixing in granite petrogenesis. Such information is rarely obtainable from the analysis of bulk rocks.*

KEY WORDS: *granite source origins; zircon Hf isotopes; zircon petrogenesis; zircon morphology; zircon U–Pb ages*

INTRODUCTION

Zircon is a common accessory mineral in a wide range of rocks, particularly in felsic igneous rocks (e.g. Heaman *et al.*, 1990; Hoskin & Schaltegger, 2003). The relationship between zircon saturation, magma crystallization and melt composition has been studied by Watson (1979) and by Watson & Harrison (1983). Their experimental work on zircon saturation showed that any felsic, non-peralkaline magma is likely to contain zircon crystals, because the saturation level is so low for magmas of this composition. The importance of this accessory mineral lies in a combination of factors, including its tendency to incorporate trace elements (including radionuclides), its chemical and physical durability, and its remarkable resistance to high-temperature diffusive re-equilibration (Watson, 1996; Watson & Cherniak, 1997). Although the abundance of zircon is low, it strongly affects the behaviour of many trace elements during the crystallization of magmas, and understanding of its chemistry therefore is important for petrological modelling (e.g. Nagasawa, 1970; Watson, 1979; Murali *et al.*, 1983).

Hafnium (Hf) is a particularly important minor element in zircon, because its isotopic composition is a sensitive tracer of crustal and mantle processes (e.g. Taylor & McLennan, 1985; Vervoort & Blichert-Toft, 1999). The basis of using the Hf isotopic ratios is the decay of ^{176}Lu to ^{176}Hf, whereas ^{177}Hf is a stable isotope. During mantle

*Corresponding author. Telephone: 61 2 9850 6126. Fax: 61 2 9850 8943. E-mail: ebelouso@els.mq.edu.au

melting, Hf is partitioned more strongly into the melts than Lu. Over time the $^{176}Hf/^{177}Hf$ therefore evolves to higher values in the mantle than in crustal rocks. During the production of granitoid magmas, high values of $^{176}Hf/^{177}Hf$ (i.e. $\varepsilon_{Hf} \gg 0$) indicate 'juvenile' mantle input, either directly via mantle-derived mafic melts, or by remelting of young mantle-derived mafic lower crust. Low values of $^{176}Hf/^{177}Hf$ ($\varepsilon_{Hf} < 0$) provide evidence for crustal reworking. Mixing of crustally-derived and mantle-derived magmas during granite production can also be detected by inhomogeneity (including zoning) in the Hf isotope composition and trace element abundances in zircon populations. Griffin *et al.* (2002) have documented wide variations in the Hf isotope composition of different zircon populations in magmatic rocks that show clear field evidence for magma mingling; the zircon preserves the chemical evidence of such mixing.

Petrologists studying magmatic rocks are confronted with the end-product of a complex evolution, but commonly there is little obvious evidence about the sequence of processes during that evolution. However, examples presented in this study show that the crystal morphology, trace element signatures, U–Pb ages and Hf isotopic compositions of magmatic zircon often contain detailed records of the evolution of individual magma chambers. The laser-ablation inductively coupled plasma mass spectrometry (LA-ICPMS) microprobe makes it possible to generate detailed trace element patterns of zircon grains from ablation pits 30–40 μm deep. This allows correlation between changes in zircon morphology and changes in the trace element chemistry, where the external morphology of zircons reflects the environment of crystallization (including magma composition and temperature). U–Pb data distinguish age populations, and the $^{176}Hf/^{177}Hf$ ratio of zircon provides a tool to assess the relative importance of mantle and crustal contributions to individual magmas and, hence, can be used to track the mechanisms that generate magmas.

In this study, magmatic zircon populations from I- and S-type granitoids from the Lachlan Fold Belt and New England Fold Belt, Eastern Australia, provide an excellent example of the usefulness of zircon in tracking petrogenetic processes, information that could not have been captured using traditional petrological and geochemical techniques.

ZIRCON AND MAGMA EVOLUTION

In addition to zircon's dominant role in controlling the abundance and distribution of zirconium and hafnium during magma evolution, it can strongly influence the behaviour of rare earth elements (REE), Y, Th, U, Nb and Ta (Murali *et al.*, 1983; Heaman *et al.*, 1990; Bea, 1996; Belousova *et al.*, 2002; Hoskin & Schaltegger, 2003). Large ionic radii and high charges make these elements incompatible in most rock-forming silicate minerals. They generally become concentrated in the residual melts, where the eventual crystallization of zircon is able to accommodate these elements. Where zircon crystallization occurs over a significant time span, compositional zoning within individual zircon grains, or differences in composition between successive generations of zircon, can record the changes in the chemical environment. The low diffusion rates of the REE and tetravalent cations (U, Th, Hf) suggest that they are essentially immobile under most geological conditions, permitting preservation of the chemical zoning and isotopic signature of each particular zircon crystal or its individual zones (e.g. Cherniak *et al.*, 1997*a*, 1997*b*; Watson & Cherniak, 1997). Some previous studies (e.g. Pupin, 1980; Krasnobayev, 1986; Wang, 1998; Berezhnaya, 1999; Wang & Kienast, 1999) have also argued for a close connection between zircon morphology and the source and evolution of the parental magma, its chemical composition and geological setting.

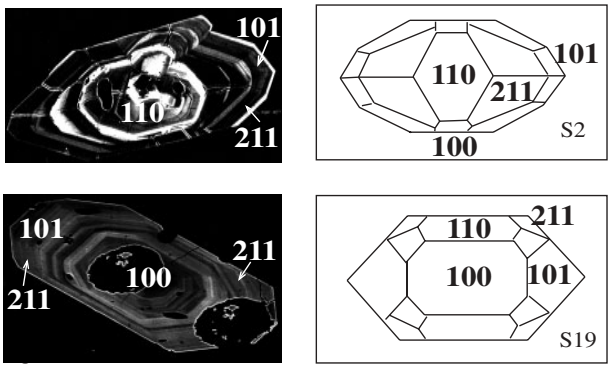

Fig. 1. Recognition of crystal forms using BSE–CL images. The laser pits in the lower photograph are about 50 μm in diameter.

Magmatic zircon commonly shows pronounced internal zoning, which can be observed in polished sections using a combination of high-resolution backscattered-electron (BSE) and cathodoluminescence (CL) imaging in the electron microprobe (Fig. 1). This zoning reflects minor compositional variations, with brighter zones enriched in U, Th, REE (Fowler *et al.*, 2002; Corfu *et al.*, 2003), and thus records changes in the external morphology of the crystal during growth. Many granitoid (*sensu lato*) magmas carry zircon grains inherited from older crustal rocks, which may represent part of the source material for the magma. These inherited grains commonly have rounded cores overgrown by euhedral magmatic zircon, easily recognized on BSE–CL images. The morphology of zircon may carry a complex record of magma history, with the development of different forms being related to both temperature and magma composition (Pupin, 1980; Wang, 1998; Corfu

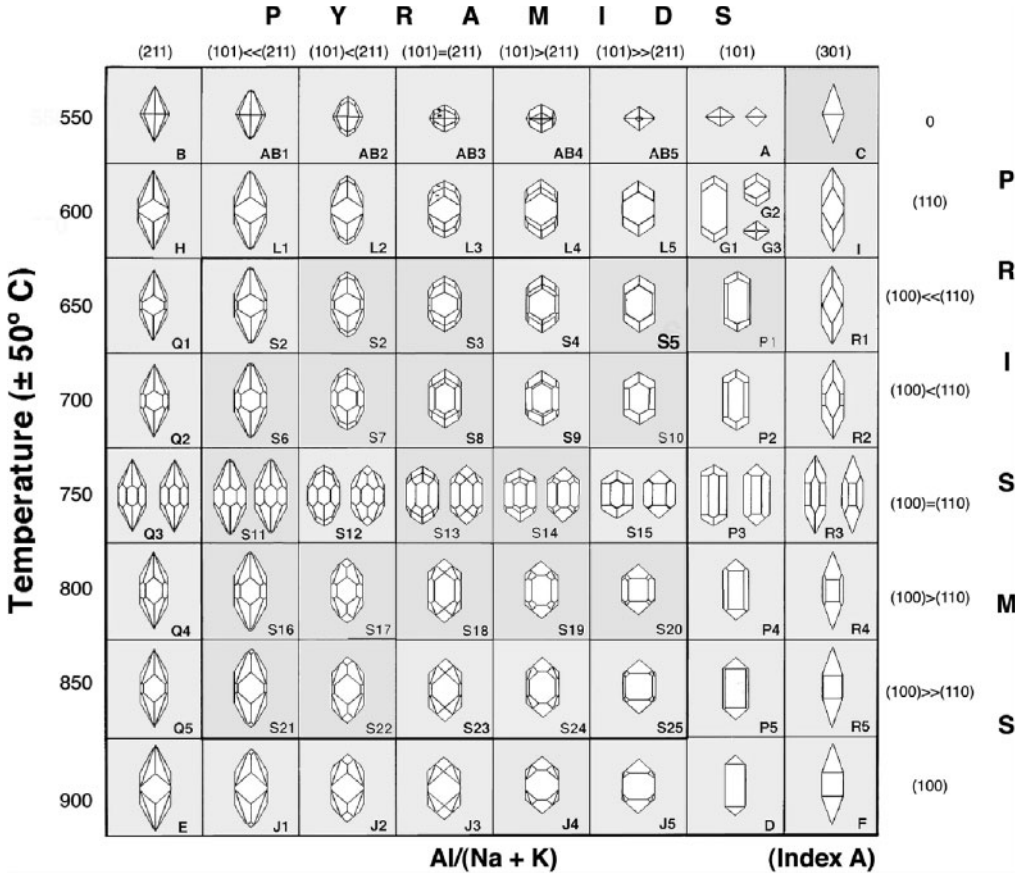

Fig. 2. Zircon typological classification and corresponding geothermometric scale proposed by Pupin (1980). Index A reflects the Al/alkali ratio, controlling the development of zircon pyramids, whereas temperature affects the development of different zircon prisms.

et al., 2003). Internal zircon zoning thus provides a qualitative record of the direction of changes in these parameters.

Changes in magma composition may result from several processes, such as fractional crystallization, degassing, or the mixing of different magmatic components (Clarke, 1992). The mixing of two magmas with different temperatures may reverse a cooling trend in one of them while accelerating the cooling of the other. If these components have different origins, their mixing may be reflected in changes in the Hf isotope composition of crystallizing zircon. Therefore, the study of zircon morphology combined with trace element chemistry and Hf isotope composition can provide valuable petrogenetic information.

The fundamental basis for the study of morphological populations in zircon was established by Pupin (1980), who argued on the basis of empirical observations that the chemical characteristics of the crystallization medium play a leading role in the relative growth of different pyramid forms. Zircon crystallized from peraluminous liquids shows well-developed {211} pyramids whereas zircon grown under peralkaline conditions has well-developed {101} pyramids; thus the Al/(Na + K) ratio is designated 'index A' (see Fig. 2). The temperature of the crystallization medium is regarded as the main factor governing the relative development of the different zircon prism forms. Therefore, this type of morphological variation was proposed by Pupin (1980) as a geothermometer, as well as a recorder of magma composition (Figs 2 and 3). Figure 3 shows the distribution of the main fields of zircon populations in the petrogenetic classification grid proposed by Pupin (1980). He recognized end-members corresponding to high-temperature, generally I-type magmas and low-temperature, generally S-type magmas, and referred to these as mantle-derived and crustal-derived, respectively (Fig. 3).

Varva (1993) has presented a more sophisticated quantitative method to describe the morphological evolution of zircon crystals, considering how the growth rates of individual faces are controlled by interface kinetics. However, in this study the simpler scheme of Pupin (1980) will be used because it provides a better visualization of the zircon typology grid (Fig. 2).

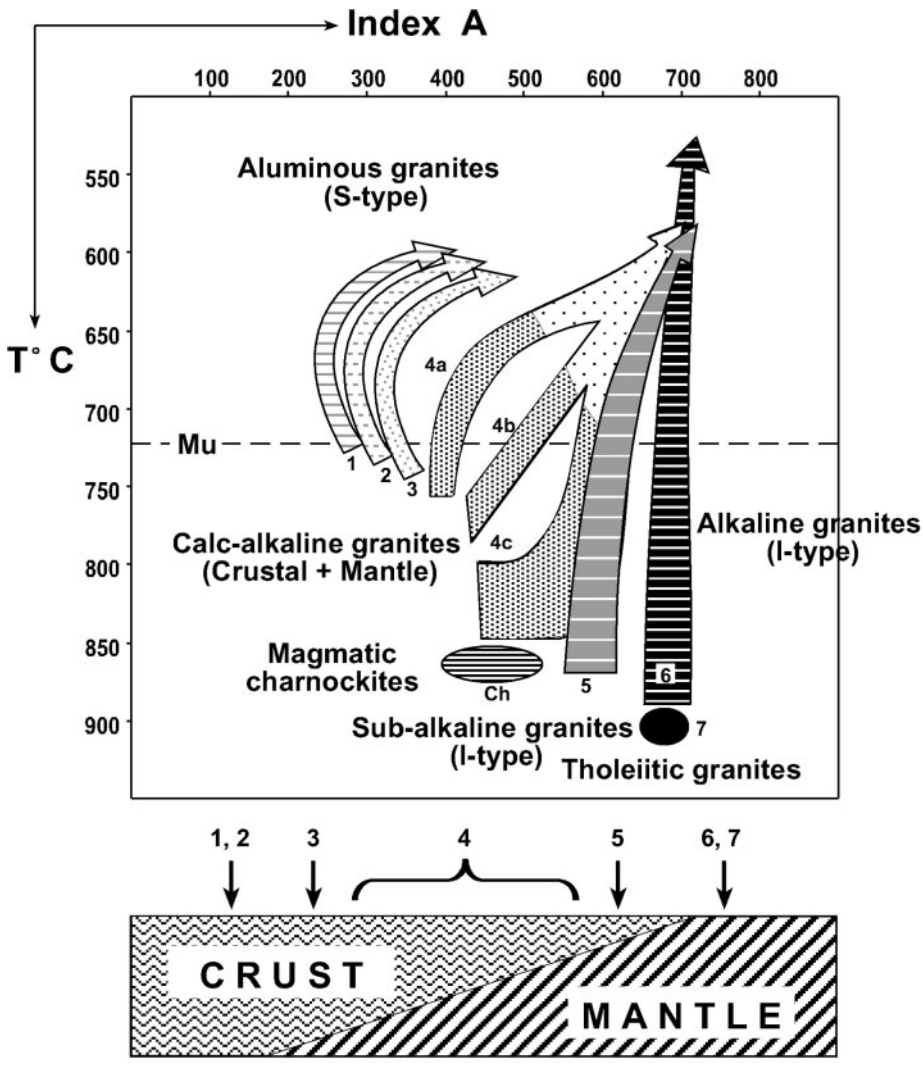

Fig. 3. Zircon populations in the petrogenetic classification proposed by Pupin (1980): (1), (2) and (3) are granites of crustal or mainly crustal origin (orogenic granites): (1) aluminous leucogranites; (2) (sub)autochthonous monzogranites and granodiorites; (3) intrusive aluminous monzogranites and granodiorites. (4) and (5) are granites of crustal + mantle origin, hybrid granites (orogenic granites): (4a–c, dark dotted area) granodiorites + monzonites; (4a–c, clear dotted area) monzogranites + alkaline granites; (5) sub-alkaline series granites. (6) and (7) are granites of mantle or mainly mantle origin (anorogenic granites): (6) alkaline series granites; (7) tholeiitic series granites. Ch, magmatic charnockite area; Mu, limit of muscovite granites (temperature <725°C). Modified from Pupin (1980).

GEOLOGICAL BACKGROUND AND SAMPLE DESCRIPTION

In this study, the evolution of magmatic systems has been tested using zircon from carefully selected I- and S-type granitoids from the Lachlan Fold Belt and New England Fold Belt, eastern Australia. The general term 'granitoid' is used in this work to simplify the definitions of the sampled rocks. Zircon from some of these locations shows very complex internal structures and the understanding of its crystallization history can provide more information on the magmatic evolution of the selected granitoids.

From seven to eleven zircon grains were carefully selected from each of the samples: the Berridale adamellite (Numbla Vale); the Kosciusko tonalite (Jindabyne); the Dundee rhyodacite ignimbrite (New England). The number of grains was limited by the requirement that each zircon should show a typical and well-recognized external crystal morphology and also was large enough to accommodate at least three laser-ablation analytical spots (trace element analysis, U–Pb dating and Hf isotopes). Grain sizes vary from about 150 to 400 μm long and from three to seven analyses were carried out on each grain, depending on the grain size and the complexity of the internal structure.

Granitoids from the Lachlan Fold Belt

The Berridale Adamellite and Kosciusko Tonalite belong to the 700 km wide Paleozoic Lachlan Fold Belt (LFB) of Eastern Australia, which is characterized by a ubiquitous Ordovician flysch cut by granitoids of different geochemical character. Chappell & White (1974, 1992) introduced the terms 'S' and 'I', which was a major contribution to granite classification at the time. They considered that the composition of granites reflects their source regions and showed that there are two contrasting granitoid types in the Kosciusko and Berridale Batholiths: the S-types derived from the partial melting of metasedimentary rocks, and the I-types from igneous sources that had not been through surface weathering processes.

Later Chappell (1996) pointed out that some granites of the LFB show clear evidence for magma mingling and mixing; however, he considered that such mixing is restricted to a small scale and was not a significant process in producing the compositional variations seen in large bodies of granite. It was concluded that restite fractionation [the restite model of White & Chappell (1977) and Chappell *et al.* (1987)] was the dominant mechanism that produced variation within the granite suites of southeastern Australia, with an important supporting role being provided by fractional crystallization.

Collins (1996) showed that the simple Nd–Sr–Pb–O isotopic arrays of these granitoids define a continuum, implying the mixing of magmatic components, and suggested that the granitoids of the Lachlan Fold Belt are the products of the mixing of three general source components: mantle, lower crust and middle crust. According to his three-component mixing model, the bimodal character of the S- and I-type granitoids of the Lachlan Fold Belt is related to the rock sequences and tectonic environment. S-type magmas are most likely to be generated in the areas of deeply underthrust Ordovician sediments; where mid-crustal geotherms exceeded the water-saturated granite solidus, typical S-type granitoids were generated. In theory, mixing between anatectic S-type magmas and intruding I-type magmas would be a rapid process. In these areas, such as the Kosciusko Batholith, I-types are rare and typically younger, because they can only intrude once the mid-crustal melt zone is depleted, and mixing with sediment is minimal.

Other models for LFB granitoid petrogenesis include a simple two-component mixing model based on the ε_{Nd-Sr} array (Gray, 1984, 1990), and a crystal fractionation model (Soesoo, 2000); the latter excludes both crustal contamination and mixing between mantle- and crustal-derived melts in the area. Knowledge of zircon crystallization history can shed more light on the evolution of the magmas and help constrain such models.

Dundee rhyodacite ignimbrite, New England Batholith

The New England Batholith is a part of the New England Fold Belt (NEFB) that underlies the northeastern part of New South Wales and eastern Queensland in eastern Australia. The NEFB is considered to have developed during Paleozoic times close to the margin of the Gondwana continent, and most of the Fold Belt is composed of mainly tholeiitic and calc-alkaline igneous rocks, sediments and subduction-accreted oceanic rocks (Leitch *et al.*, 1988). The Dundee rhyodacite ignimbrite belongs to the Moonbi Supersuite exposed in the area to the east of Tamworth. Geochemically the granitoids of this suite are recognized as having the distinct characteristics of I-type granitoids (Shaw & Flood, 1981).

ANALYTICAL METHODS

Zircon grains were hand-picked under a binocular microscope, mounted in a thin layer of epoxy on petrographic slides, and polished down to about half of their thickness for analysis. Prior to analytical work, polished surfaces were examined for zoning and backscattered electron–cathodoluminescence (BSE–CL) images were taken on the electron microprobe. Two or three analytical points for trace element composition, and 1–3 points for Hf and U–Pb isotope composition have been studied for each grain. BSE–CL images have been made before and after the analysis to evaluate which analyses best represent each zone (examples of core and rim laser pits are shown in Fig. 1).

All analyses were carried out in the Geochemical Analysis Unit (GAU) in the GEMOC Key Centre in the Department of Earth and Planetary Sciences, Macquarie University.

Electron microprobe

Hf contents of the zircons were determined by the CAMEBAX SX50 electron microprobe so that Hf could be used as the internal standard for trace element determination by LA-ICPMS. An accelerating voltage of 15 kV and a beam current of 20 nA were used for all analyses. The spatial resolution of the electron microprobe is ~2 μm. The detection level for Hf was 0·12% with a precision of 2·5% RSD at 1·5% HfO_2.

Combined BSE–CL observations were made using the same electron microprobe with operating conditions of 15 kV accelerating voltage and 15–20 nA beam current. The images are a combination of BSE and CL phenomena obtained by operating the BSE detector at high gain amplification, where the BSE image reflects the difference in the mean atomic number of elements in the mineral chemical composition and cathodoluminescence

is produced by the irradiation of the zircon with the electron beam.

Trace element determinations

Trace element content was analysed by a UV laser ablation microprobe coupled to either a Perkin–Elmer ELAN 5100 ICPMS system or a Perkin–Elmer ELAN 6000 ICPMS system. Detailed descriptions of instrumentation, analytical and calibration procedures have been given by Norman *et al.* (1996, 1998). The laser ablation system is a Continuum Surelite I-20 Q-switched Nd:YAG laser with a fundamental infrared (IR) wavelength at 1064 nm and a pulse width of 5–7 ns. Two frequency doubling crystals provide second and fourth harmonics in the visible (VIS, 532 nm) and ultraviolet (UV, 266 nm), respectively. The 266 nm beam was used for the trace element analyses reported here. Most of the analyses were carried out with a pulse rate of 4 Hz (pulses per second) and a beam energy of 1 mJ/pulse, producing a spatial resolution of 30–50 μm.

Quantitative results for 24 elements reported here were obtained through calibration of relative element sensitivities using the NIST-610 standard glass as the external calibration standard, and normalization of each analysis to the electron-probe data for Hf as an internal standard. The precision and accuracy of the NIST-610 analyses are 2–5% for REE, Y, Sr, Nb, Hf, Ta, Th and U at the ppm concentration level, and from 8% to 10% for Mn, P, Ti and Pb.

Hf isotope determination

Hf isotope analyses were carried out *in situ* with either a Merchantek/New Wave Research 213 nm or a 193 nm EXCIMER laser-ablation microprobe, attached to a Nu Plasma multi-collector ICPMS system. A 5 Hz repetition rate, 30% iris setting, and energies of about 0·2 mJ/pulse were the operation conditions when using the Merchantek 213 laser. A 2 Hz repetition rate and about 0·05 mJ energy with 0·4 J/cm^2 power density were used with the 193 nm EXCIMER laser. Most analyses were carried out with a beam diameter of ~50 μm. Typical ablation times were 80–120 s, resulting in pits 40–50 μm deep. The methods and analyses of standard solutions and standard zircons have been described by Griffin *et al.* (2000).

For the calculation of ε_{Hf} values, we have adopted the chondritic values of Blichert-Toft *et al.* (1997). These values were reported relative to $^{176}Hf/^{177}Hf = 0{\cdot}282163$ for the JMC475 standard, well within error of our previously reported value (Griffin *et al.*, 2000, 2004). To calculate model ages (T_{DM}) based on a depleted-mantle source, we have adopted a model with $(^{176}Hf/^{177}Hf)_i = 0{\cdot}279718$ and $^{176}Lu/^{177}Hf = 0{\cdot}0384$; this produces a value of $^{176}Hf/^{177}Hf$ (0·28325) similar to that of average mid-ocean ridge basalt (MORB) over 4·56 Gyr. There are currently three proposed values of the decay constant for ^{176}Lu. ε_{Hf} values and model ages reported here (Tables 1–3) were calculated using the value ($1{\cdot}93 \times 10^{-11}$ year^{-1}) proposed by Blichert-Toft *et al.* (1997), because this number is close to the average value of the other two recently reported values ($1{\cdot}865 \times 10^{-11}$ year^{-1}, Scherer *et al.*, 2001; $1{\cdot}983 \times 10^{-11}$ year^{-1}, Bizzarro *et al.*, 2003).

T_{DM} ages, which are calculated using the measured $^{176}Lu/^{177}Hf$ of the zircon, can only give a minimum age for the source material of the magma from which the zircon crystallized. Therefore we also have calculated, for each zircon, a 'crustal' model age (T_{DM}^{C}, Tables 1–3), which assumes that its parental magma was produced from an average continental crust ($^{176}Lu/^{177}Hf = 0{\cdot}015$) that originally was derived from the depleted mantle.

U–Pb dating

The data reported here were obtained using an Agilent 4500 series 300 ICPMS system, coupled to a Merchantek/New Wave Research 213 nm microprobe at GEMOC, Macquarie University, Sydney. A description of the procedure has been given by Jackson *et al.* (2004). The repetition rate used for all analyses was 5 Hz, the aperture beam diameter–iris setting is 15%, beam expander is zero and the incident pulse energy is about 0·08–0·1 mJ. The spot size for most of the 213 nm laser analyses is about 40–50 μm.

Data were acquired on five isotopes (^{206}Pb, ^{207}Pb, ^{208}Pb, ^{232}Th, ^{238}U) using the instrument's time-resolved analysis data acquisition software. This data acquisition protocol allows acquisition of signals as a function of time (ablation depth), and subsequent recognition of isotopic heterogeneity within the ablation volume (e.g. zones of Pb loss or common Pb related to fractures or areas of radiation damage; also inclusions, inherited cores, etc.). The signals can then be selectively integrated. Useful data cannot be acquired for ^{204}Pb because of the large isobaric interference from Hg, a significant contaminant in the Ar supply. Hg signals could not be reduced sufficiently using either activated charcoal or gold filters to allow useful analyses.

A fast peak-hopping protocol (dwell time per isotope from 10 to 30 ms) resulted in a full mass sweep time of ~100 ms, allowing representative measurement of rapidly transient signals typical of laser ablation sampling. Each 2·5 min analysis consisted of ~60 s of measurement of instrumental background (i.e. analysis of carrier gas, no ablation) followed by the ablation event.

Mass discrimination of the mass spectrometer and residual elemental fractionation were corrected by calibration against a homogeneous standard zircon,

Table 1: Trace element and isotopic data for zircons from kosciusko tonalite

Population:	Inherited/or grain's core							Type 1				Type 2						
Analysis no.:	2-core	3-core	5-core	6-core	9-core	11-core	12-cor	1	6-rim	8-rim	11-rim	4	5-rim	7	8-core	9-rim	10	12-rim
Trace element data (ppm)																		
P	305	211	156	283	386	142	1780	411	147	310	166	446	223	843	314	1480	341	584
Ti	<34	880	<31	<48	28	<35	41	<40	<29	72	39	4060	32	317	<31	61	<27	<30
Mn	<7	348	<4·2	<6·9	15	<4·9	12	<5·4	<3·9	15	<4·1	254	7·7	60	<5·8	8·3	<5·7	13
Sr	<0·71	26	<0·63	1·9	1·7	<1·1	2·0	<0·51	<1·0	4·8	<0·93	7·7	1·6	40	<0·8	4·5	0·72	3·7
Y	1210	1330	374	1740	1620	658	1020	1910	515	1060	661	546	683	4090	1180	4250	688	827
Nb	<1·22	9·6	1·3	<1·5	2·6	2·0	2·5	3·6	2·2	3·6	1·8	<0·96	1·4	31	3·2	4·6	2·7	3·2
Ba	<0·85	74	<0·39	2·1	7·5	<0·49	0·57	0·56	<0·82	27	<0·67	17	5·7	20	<0·49	3·6	<0·61	49
La	<0·58	61	2·3	1·1	4·0	8·3	7·0	<0·34	<0·42	2·1	<0·40	41	6·2	447	0·83	46	1·9	20
Ce	9·3	112	11	25	13	63	26	17	10	19	16	31	15	918	12	115	16	53
Pr	0·47	19	0·99	2·5	2·2	5·0	1·9	<0·29	<0·33	<0·39	<0·24	8·6	2·2	224	0·67	25	0·61	9·3
Nd	2·0	74	5·7	6·8	13	35	15	2·9	<2·2	2·1	2·1	40	13	1250	<2·1	139	6·3	54
Sm	3·7	19	<1·6	6·7	10	17	5·7	4·1	<2·4	<2·6	2·9	5·7	<3·3	446	3·0	58	<2·6	25
Eu	<0·79	2·9	0·70	<0·96	0·81	3·3	0·87	1·1	<0·76	0·61	0·51	0·82	0·89	5·2	<1·1	6·3	<0·61	2·6
Gd	21	33	<2·0	32	31	32	17	25	7·6	9·0	9·1	11	11	408	16	77	11	22
Dy	102	118	24	137	134	63	68	146	36	77	46	41	45	445	83	316	48	56
Ho	40	44	10	55	53	20	30	62	17	32	19	16	20	136	37	140	22	24
Er	197	197	59	271	241	87	163	300	81	168	98	83	120	558	196	666	113	129
Yb	359	383	164	469	434	180	379	642	207	438	272	221	301	1210	451	1440	293	351
Lu	81	77	41	102	88	38	95	143	49	95	67	49	68	225	108	288	68	84
Hf (wt %)	0·92	0·89	1·06	1·32	0·83	1·3	0·97	1·02	1·07	1·54	1·29	0·88	1·40	1·30	1·12	1·15	1·00	1·30
Ta	0·87	1·4	0·74	1·4	0·84	0·78	1·4	1·3	0·80	1·4	0·63	0·64	1·1	11	0·77	2·1	0·94	2·3
Pb	<1·8	28	3·5	6·2	4·0	13	8·6	7·2	<2·2	6·9	5·9	6·6	3·4	18	3·2	3·5	4·3	8·4
Th	69	133	74	257	165	444	204	244	93	148	156	115	120	3780	144	679	211	317
U	117	281	200	371	702	367	308	416	183	337	318	663	241	2060	291	1040	313	725

Table 1: continued

Population:	Inherited/or grain's core							Type 1				Type 2						
Analysis no.:	2-core	3-core	5-core	6-core	9-core	11-core	12-core	1	6-rim	8-rim	11-rim	4	5-rim	7	8-core	9-rim	10	12-rim
Lu–Hf isotope data																		
$^{176}Hf/^{177}Hf$	0·28344	0·28258		0·28248	0·28243			0·28243		0·28290		0·28242	0·28240		0·28247	0·28244	0·28240	
±1SE	0·00002	0·00002		0·00003	0·00002			0·00002		0·00001		0·00002	0·00002		0·00001	0·00002	0·00001	
$^{176}Lu/^{177}Hf$	0·00095	0·00210		0·00115	0·00090			0·00157		0·00072		0·00097	0·00067		0·00166	0·00249	0·00059	
$^{176}Yb/^{177}Hf$	0·04190	0·10112		0·05836	0·04071			0·07123		0·02795		0·04143	0·02807		0·07157	0·11180	0·02263	
$^{176}Hf/^{177}Hf$ average	0·28248 ± 0·00007							0·28242 ± 0·00003				0·28243 ± 0·00003						
*Model age**																		
ε_{Hf}	−2·65	2·02		−1·25	−2·74			−2·89		−3·96		−3·22	−3·95		−1·65	−2·88	−3·82	
T_{DM} (Ga)	1·11	0·95		1·06	1·12			1·14		1·16		1·14	1·16		1·09	1·15	1·15	
T_{DM} (crustal)	1·54	1·25		1·45	1·54			1·55		1·62		1·57	1·62		1·48	1·55	1·61	
U–Pb data; $^{206}Pb/^{238}U$ weighted average = 418 ± 4 Ma (MSWD = 0·63; n = *9)*																		
$^{206}Pb/^{238}U$	421	382		439				421	430	421	411	411		489	422	418	420	419
±2σ	12	11		11				11	12	11	12	11		13	11	11	12	11
$^{207}Pb/^{206}Pb$	495	562		506				412	633	452	369	467		501	452	436	429	464
±2σ	109	89		53				57	83	55	95	61		48	55	49	77	59
$^{207}Pb/^{235}U$	432	408		450				419	464	426	405	420		491	427	421	406	426
±2σ	18	15		10				10	15	10	15	11		11	10	9	13	11
$^{208}Pb/^{232}Th$	455	461		521				429	504	412	408	455		435	419	222	409	420
±2σ	22	19		13				11	20	11	17	13		11	11	7	15	11
Comments		Pb loss		Common Pb				Common Pb								Inherited		

*Blichert-Toft *et al.* (1997) ^{176}Lu decay constant ($1{\cdot}93 \times 10^{-11}$) has been used for these calculations.

Table 2: Trace element and isotopic data for zircons from the Berridale adamellite

Population:	Inherited	Type 1		Type 2			Type 3	Type 4			
Analysis no.:	5	3-core	9-core	9-rim	3-rim1	3-rim2	6	1-rim	2	4-rim	8-rim
Trace element data (ppm)											
P	158	186	175	205	545	1060	412	270	759	797	756
Ti	59	<88	<67	<71	<58	<48	<47	<29	<86	<55	<64
Mn	—	433	—	—	37	57	8·4	11	—	51	—
Sr	1·2	6·6	1·2	<1·1	6·2	10	<1·7	2·8	<1·5	<2·2	<1·5
Y	2110	1890	1470	826	1590	982	3710	815	2850	2405	2500
Nb	2·7	<2·6	<2·8	<1·5	2·0	4·2	5·6	2·4	3·3	2·9	2·4
Ba	<0·96	7·2	<1·1	<0·90	17	36	<1·3	1·4	13	2·6	1·2
La	<1·0	5·3	<1·1	<0·72	164	12	<0·89	93	<1·2	4·5	<1·2
Ce	11	61	17	12	354	52	42	149	5·8	21	5·5
Pr	1·0	5·2	3·3	<0·42	32	5·7	<0·88	18	<0·92	3·3	<0·57
Nd	19	30	<8·5	<2·7	159	29	13	73	<5·5	21	<6·5
Sm	20	21	5·8	<4·9	38	12	18	14	<10	12	<7·1
Eu	<2·2	2·3	1·6	<1·6	2·1	<1·5	2·1	<1·3	<2·2	1·8	<3·0
Gd	74	64	32	11	63	27	74	20	27	34	27
Dy	249	204	136	72	173	94	378	68	197	190	189
Ho	71	67	48	27	52	29	127	25	90	82	82
Er	299	260	243	148	233	139	562	130	490	396	380
Yb	632	664	637	474	644	405	1080	486	1170	902	831
Lu	81	102	104	71	82	64	154	63	228	161	164
Hf (wt %)	0·78	1·21	1·06	1·12	1·36	0·91	1·04	1·28	1·19	1·20	1·24
Ta	<1·2	1·2	<1·2	2·0	4·2	1·4	2·8	1·8	3·4	1·9	<1·3
Pb	<3·7	20	8·8	<3·2	32	4·6	19	4·3	5·7	<3·4	<4·2
Th	64	605	284	148	906	218	608	260	110	136	81
U	74	1491	611	578	2190	964	673	1210	696	535	449

Table 2: continued

Population:	Inherited	Type 1		Type 2			Type 3	Type 4			
Analysis no.:	5	3-core	9-core	9-rim	3-rim1	3-rim2	6	1-rim	2	4-rim	8-rim
Lu–Hf isotope data											
$^{176}Hf/^{177}Hf$	0·28255	0·28223	0·28226	0·28233		0·28229	0·28243	0·28228	0·28240	0·28243	0·28241
±1SE	0·00002	0·00002	0·00002	0·00002		0·00002	0·00003	0·00002	0·00003	0·00002	0·00003
$^{176}Lu/^{177}Hf$	0·00143	0·00111	0·00110	0·00141		0·00173	0·00137	0·00114	0·00199	0·00219	0·00220
$^{176}Yb/^{177}Hf$	0·07491	0·05164	0·04786	0·05970		0·07561	0·05790	0·04830	0·09744	0·10362	0·10080
$^{176}Hf/^{177}Hf$ average		0·28225 ± 0·00002		0·28231 ± 0·00003				0·28238 ± 0·00007			
*Model age**											
ε_{Hf}	1·59	−9·61	−8·40	−6·30		−7·85	−2·75	−7·92	−4·91	−2·78	−3·49
T_{DM} (Ga)	0·97	1·40	1·35	1·28		1·35	1·14	1·33	1·24	1·16	1·19
T_{DM} (crustal)	1·29	1·98	1·90	1·78		1·87	1·56	1·87	1·69	1·56	1·60
U–Pb data; $^{206}Pb/^{238}U$ weighted average = 435 ± 5 Ma (MSWD = 0·044; n = *6)*											
$^{206}Pb/^{238}U$	1090	508	461	433	448	435	435	436	434	428	436
±2σ	28	13	12	11	11	11	11	11	12	6	11
$^{207}Pb/^{206}Pb$	1152	512	502	441	447	469	526	390	440	882	571
±2σ	64	46	61	57	45	47	53	56	57	23	45
$^{207}Pb/^{235}U$	1111	508	468	434	447	441	450	429	435	507	458
±2σ	24	11	12	11	9	9	11	10	11	6	10
$^{208}Pb/^{232}Th$	1139	536	569	472	482	459	472	459	446	236	166
±2σ	33	12	17	13	11	11	11	13	17	3	4
Comments	Inherited	Older core	Older core		Core–rim mix					Common Pb & Pb loss	

*Blichert-Toft *et al.* (1997) ^{176}Lu decay constant ($1{\cdot}93 \times 10^{-11}$) has been used for these calculations.

Table 3: Trace element and isotopic data for zircons from Dundee Rhyodacite, New England

Population:	Type 1		Type 2								Type 3		
Analysis no.:	1-core	4-core	1-rim	2-rim	3-core	4-rim	5-core	5-rim	7-core	7-rim	3-rim	6-core	6-rim
Trace element data (ppm)													
P	1010	425	1550	5530	1660	1040	338	561	302	633	675	483	566
Ti	<34	32	<32	<42	141	<56	<61	<37	<49	<21	26	<33	<19
Mn	<7·1	<8·8	27	57	14	27	<28	<19	<7·5	<5·6	<11	<14	5·6
Sr	<174	<8·0	5·5	19	6·8	4·8	<5·3	3·6	<5·3	0·95	<1·2	<1·0	1·3
Y	3070	1295	1300	1250	1460	1580	999	1570	1490	1110	1050	1645	1290
Nb	<4·0	2·8	4·9	5·4	1·3	6·5	<7·6	3·6	5·4	4·8	2·9	3·1	6·7
Ba	<8·9	<3·7	<1·3	<5·3	3·5	3·3	<2·1	2·0	0·60	<0·60	1·5	6·5	3·5
La	2·4	2·1	28	114	30	8·6	1·9	4·1	1·5	9·0	1·5	3·8	6·9
Ce	3·8	13	79	324	88	45	16	41	12	41	21	24	42
Pr	4·1	2·0	8·8	40	14	6·9	1·9	3·1	1·3	3·5	2·1	3·5	3·1
Nd	16	9·0	53	165	66	20	3·5	10	2·2	24	3·5	9·6	14
Sm	9·9	9·8	22	32	23	6·3	21	10	5·7	7·1	7·7	9·0	9·3
Eu	2·6	1·0	1·6	3·5	4·4	1·4	2·9	0·87	2·5	0·66	1·0	1·5	0·74
Gd	45	21	23	52	44	27	18	26	31	20	21	29	16
Dy	250	102	109	107	124	134	72	134	130	92	87	142	96
Ho	102	41	45	41	50	51	31	51	52	37	34	53	39
Er	482	200	211	201	233	258	152	230	241	176	153	262	196
Yb	821	360	422	414	385	488	306	466	428	373	328	480	438
Lu	178	80	92	82	84	106	63	102	95	87	74	98	103
Hf (wt %)	1·19	1·26	1·39	1·23	1·02	1·60	1·22	1·50	1·22	1·40	1·61	1·33	1·35
Ta	<2·4	<1·2	3·2	1·8	4·7	9·1	<7·1	1·8	0·80	1·9	2·1	<1·7	1·8
Pb	<5·2	8·2	8·1	<5·2	3·6	<5·0	<4·6	<5·4	2·9	5·4	4·2	3·1	8·4
Th	70	419	313	306	182	321	190	352	224	317	204	313	375
U	217	489	645	545	268	575	284	591	323	601	379	408	673

Table 3: continued

Population:	Type 1		Type 2								Type 3		
Analysis no.:	1-core	4-core	1-rim	2-rim	3-core	4-rim	5-core	5-rim	7-core	7-rim	3-rim	6-core	6-rim
Lu–Hf isotope data													
$^{176}Hf/^{177}Hf$	0·28287	0·28282	0·28285	0·28286	0·28275	0·28277	0·28287	0·28282	0·28283	0·28282	0·28283	0·28278	0·28275
±1SE	0·00002	0·00002	0·00002	0·00002	0·00002	0·00002	0·00002	0·00002	0·00002	0·00002	0·00002	0·00002	0·00002
$^{176}Lu/^{177}Hf$	0·00210	0·00161	0·00095	0·00052	0·00113	0·00102	0·00193	0·00099	0·00106	0·00088	0·00066	0·00097	0·00080
$^{176}Yb/^{177}Hf$	0·07289	0·05603	0·02965	0·01616	0·03686	0·03234	0·06850	0·03063	0·03467	0·02895	0·02051	0·03302	0·02698
$^{176}Hf/^{177}Hf$ average	0·28285 ± 0·00003		0·28282 ± 0·00004								0·28279 ± 0·00004		
*Model age**													
ε_{Hf}	8·80	7·36	8·58	8·86	4·69	5·41	8·79	7·47	7·74	7·31	7·71	5·95	4·96
T_{DM} (Ga)	0·55	0·60	0·55	0·53	0·70	0·67	0·54	0·59	0·58	0·59	0·58	0·65	0·68
T_{DM} (crustal)	0·71	0·80	0·72	0·70	0·96	0·92	0·71	0·79	0·77	0·80	0·78	0·88	0·95
U–Pb data; $^{206}Pb/^{238}U$ weighted average = 257·6 ± 2·5 Ma (MSWD = 0·70, probability = 0·65, n = 7)													
$^{206}Pb/^{238}U$	267	291	268	255	255	259	261		261		255	263	
±2σ	7	8	7	7	7	7	7		7		7	7	
$^{207}Pb/^{206}Pb$	732	964	747	397	277	279	306		291		361	1119	
±2σ	69	51	62	76	79	68	79		62		89	50	
$^{207}Pb/^{235}U$	321	380	324	269	257	260	266		264		266	371	
±2σ	10	9	9	9	9	9	9		7		10	9	
$^{208}Pb/^{232}Th$	340	300	310	264	251	263	230		237		269	304	
±2σ	11	7	9	8	8	7	7		6		9	7	
Comments	Common Pb	Common Pb	Common Pb				Core–rim mix		Core–rim mix			Common Pb	

*Blichert-Toft *et al.* (1997) ^{176}Lu decay constant ($1·93 \times 10^{-11}$) has been used for these calculations.

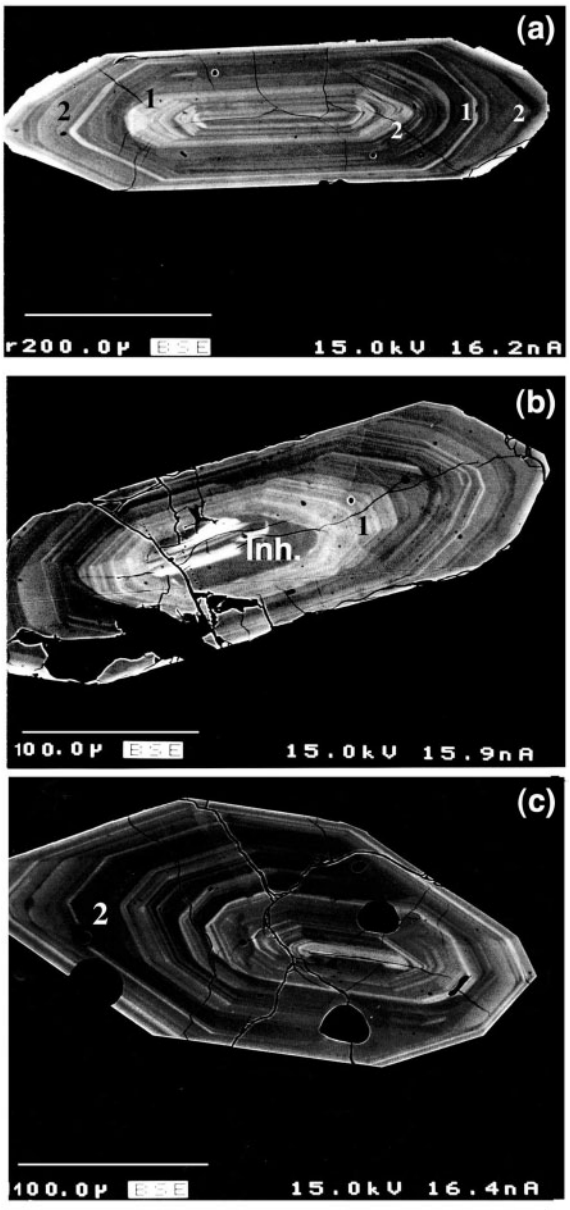

Fig. 4. BSE–CL images of zircon grains from the Kosciusko tonalite, Jindabyne. (a) Sample 7959-111-1; (b) sample 7959-111-11; (c) sample 7959-111-4. Numbers indicate zircon morphological types and 'Inh' an inherited core.

GEMOC/GJ-1 (609 Ma). Samples are analysed in 'runs' of ~20 analyses, which include 12 unknowns, bracketed, beginning and end, by two to four analyses of the standard. The 'unknowns' include two near-concordant standard zircons, 91500 (Wiedenbeck *et al.*, 1995) and Mud Tank (Black & Gulson, 1978), which are analysed in every run as an independent control on reproducibility and instrument stability. The precision and accuracy obtained on those standards, and several others, by LA-ICPMS have been discussed in detail by Jackson *et al.* (2004).

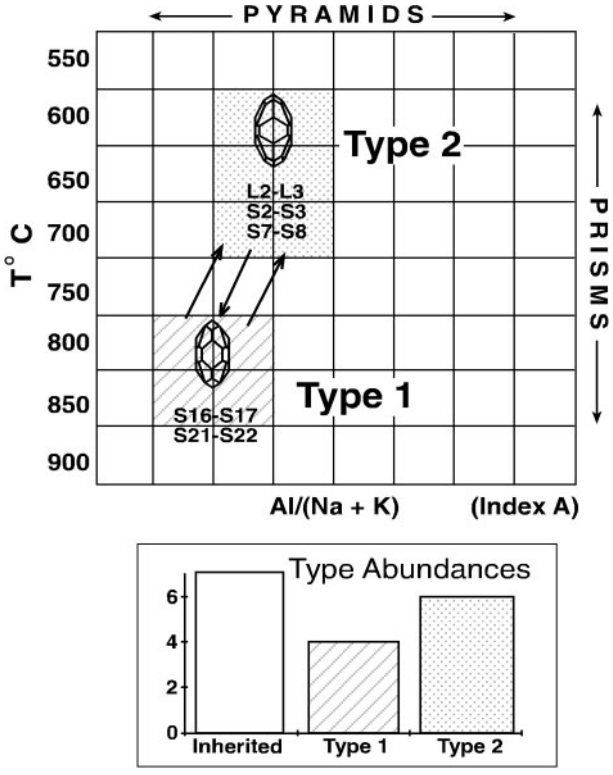

Fig. 5. Morphological types of zircon from the Kosciusko S-type tonalite.

RESULTS

Zircon crystal morphology

Morpological studies are commonly conducted on unmounted grains, and are based on the three-dimensional morphology of the grain surface. However, in this work the zircon crystal morphology was studied after zircon grains were polished to expose their centers and imaged. The use of BSE–CL images gives the advantage of showing not only external but also internal morphology, and thus makes it possible to trace changes in the grain's morphology during crustal growth. Figure 1 shows an example of recognition of the main zircon crystal forms using BSE–CL images. The recognition of two main zircon pyramids and prisms allows the discrimination of zircon morphological types using the Pupin (1980) classification as shown in Figures 2 and 3.

Kosciusko tonalite

There are two morphological types recognized in this sample (Fig. 4). Type 1 zircons (Fig. 4a and b) show a well-developed {100} prism and two pyramids, {101} and {211}, with the latter more dominant. They belong to subtypes S16–S17 and/or S21–S22 of Pupin's typological classification (Fig. 5). Such morphological forms are

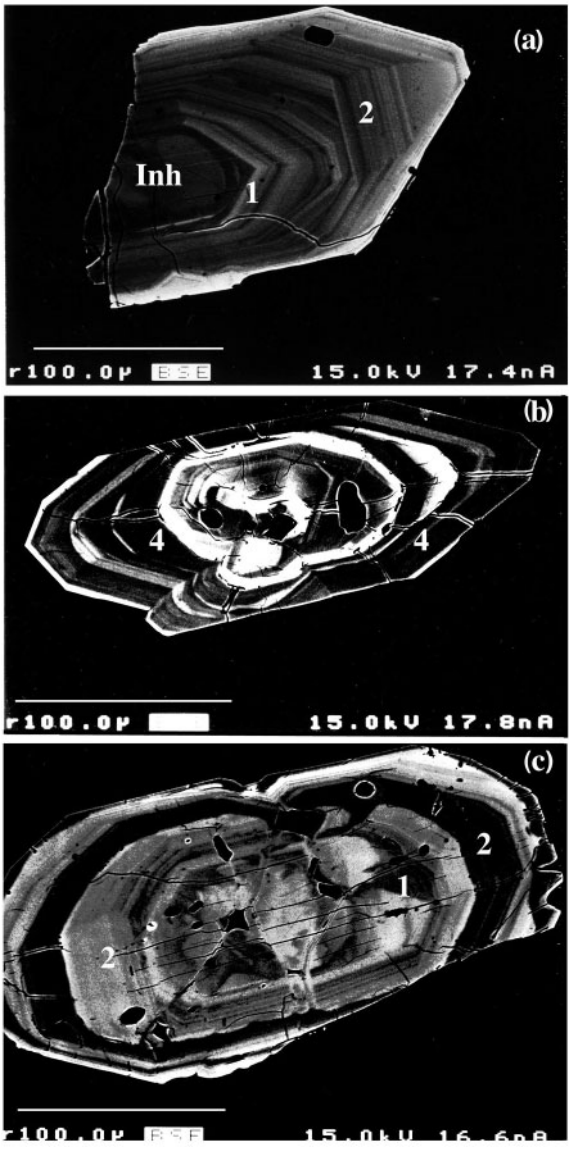

Fig. 6. BSE–CL images of zircon grains from the Berridale adamellite, Numbla Vale. (a) Sample 7955-113-9; (b) sample 7955-113-4; (c) sample 7955-113-3. Numbers indicate zircon morphological types and 'Inh' an inherited core.

common in zircon from tonalites. Type 2 zircons from the Kosciusko tonalite have a well-developed {110} prism and two pyramids, {101} and {211}, with the pyramid {211} more dominant (Fig. 5). They correspond to subtypes L2–L3 and/or S2–S3 and/or S7–S8. This morphological type is more typical of zircon from aluminous monzogranites and granodiorites.

In general, type 1 zircons are overgrown by type 2, but rare overgrowths of type 2 by type 1 are also observed. In addition, inherited cores with rounded or subrounded outlines are also easily recognized on BSE images.

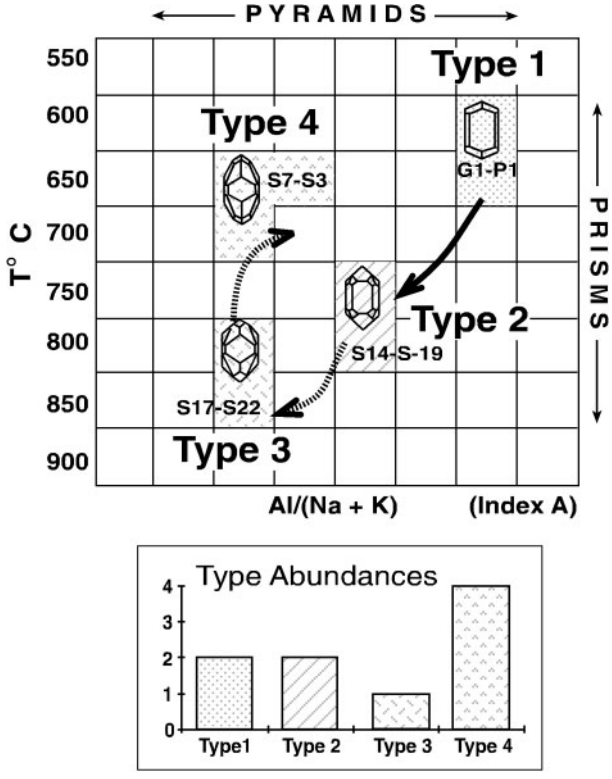

Fig. 7. Morphological types of zircon from the Berridale S-type adamellite. Continuous-line arrow connects populations with evidence of overgrowth and a dashed arrow is used if there is no evidence of such overgrowths.

Berridale adamellite

Zircon grains from the Berridale adamellite form four distinct morphological types (Figs 6 and 7). Type 1 (Fig. 6a and c) is typical of zircon populations formed in sub-alkaline and alkaline series granitoids of crustal-plus-mantle or mainly mantle origin, according to the genetic classification (Figs 3 and 7). They have a well-developed prism {110} and pyramid {101} forms (subtypes G_1 and P_1). Type 2 zircons (Fig. 6c) show a predominance of {100} prism forms and the presence of two pyramids, one weakly developed {211} and the other well developed {101} (subtypes S_{14} and S_{19}). This morphological type, according to Pupin's scale, is characteristic of calc-alkaline granodiorites of hybrid (crustal and mantle) origin (Figs 3 and 7).

Type 3 zircon crystals have two well-defined prisms and two pyramids. Faces {100} and {211} are slightly predominant (subtypes S_{17} and S_{22}; Figs 3 and 7). This type of zircon is typical of tonalitic rocks and represents the highest temperature of crystallization among the zircon of this sample. Pupin (1980) suggested that the host rock of this zircon type could form by anatexis of amphibole-bearing metamorphic rocks. Type 4 (Fig. 6b) is the most abundant group, and has a well-developed {110}

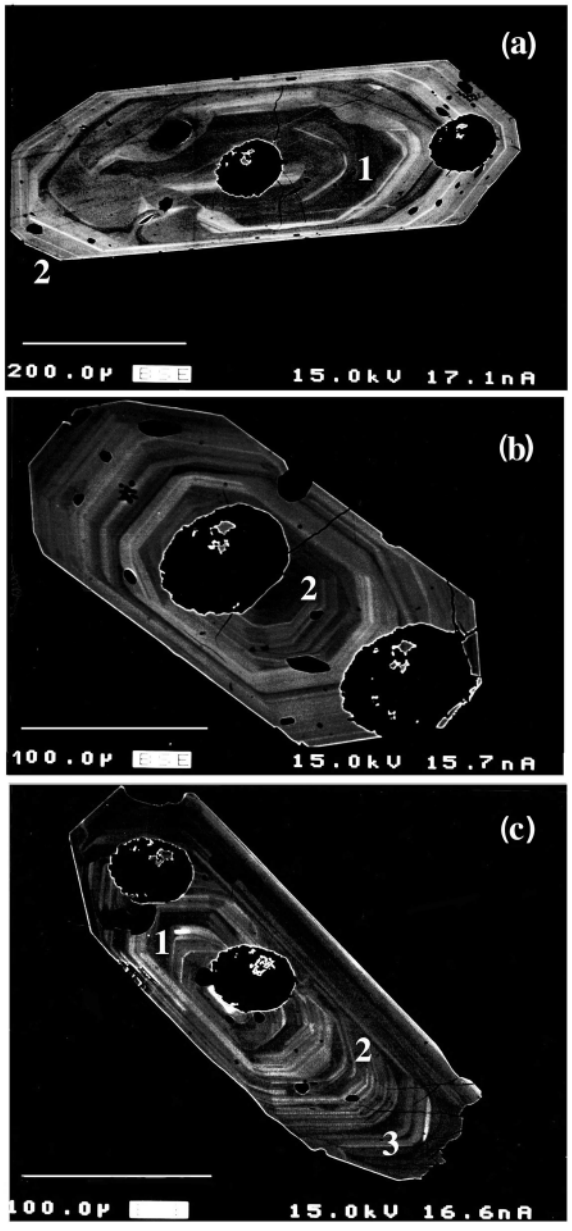

Fig. 8. BSE–CL images of zircon grains from the Dundee rhyodacite ignimbrite, New England. (a) Sample NEB191-1; (b) sample NEB191-7; (c) sample NEB191-3. Numbers indicate zircon morphological types. The holes on grains are pits from the laser ablation microprobe.

prism and {211} pyramid. The {100} prism and {101} pyramid are subordinate (subtypes S_3, S_4, S_8; Figs 3 and 7). This type is common in aluminous granodiorites of crustal or mainly crustal origin.

There is clear evidence in the BSE–CL images of zircon type 1 overgrown by type 2, but there is no evidence for the crystallization order of types 2, 3 and 4. Besides those four types, inherited zircons are also found in the cores of the zircon grains. They have

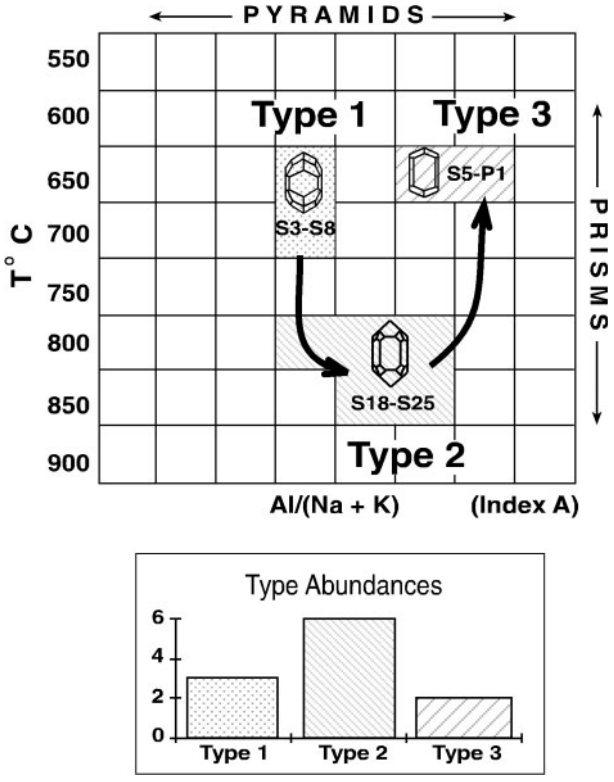

Fig. 9. Morphological types of zircon from the Dundee I-type rhyodacite ignimbrite.

rounded or ellipsoidal outlines, sometimes with resorption features (Fig. 6a), and have no evident faces.

Dundee rhyodacite ignimbrite

Zircon from the Dundee rhyodacite ignimbrite can be separated into three morphological types (Fig. 8). Type 1 (Fig. 8a and c) shows morphological features common in zircon from aluminous monzogranites and granodiorites of mainly crustal origin (Figs 3 and 9). They are subtypes S_3–S_8, having a well-developed {110} prism and equally well-developed {101} and {211} pyramids. The faces frequently show evidence of partial resorption (Fig. 8a), producing rounded surfaces or embayments. Type 2 zircon (Fig. 8b and c) is the most common morphological type in the Dundee rhyodacite ignimbrite. The crystal morphology is very distinctive, having a well-developed {100} prism and {101} pyramid with supplementary {211} pyramid and {110} prism (subtypes S_{18}, S_{19}, S_{20}, S_{24} and S_{25}; Fig. 9) typical of zircon found in calc-alkaline granodiorites or sub-alkaline granitoids. The source rock, according to Pupin's scheme, could be a hybrid of mantle and crustal origin (Fig. 3). Type 3 (Fig. 8c) represents a relatively small group; crystals show a well-developed {110} prism and a single {101} pyramid (subtype P_1 and S_5; Fig. 9), typical of zircon from 'granitoids of mainly mantle origin'.

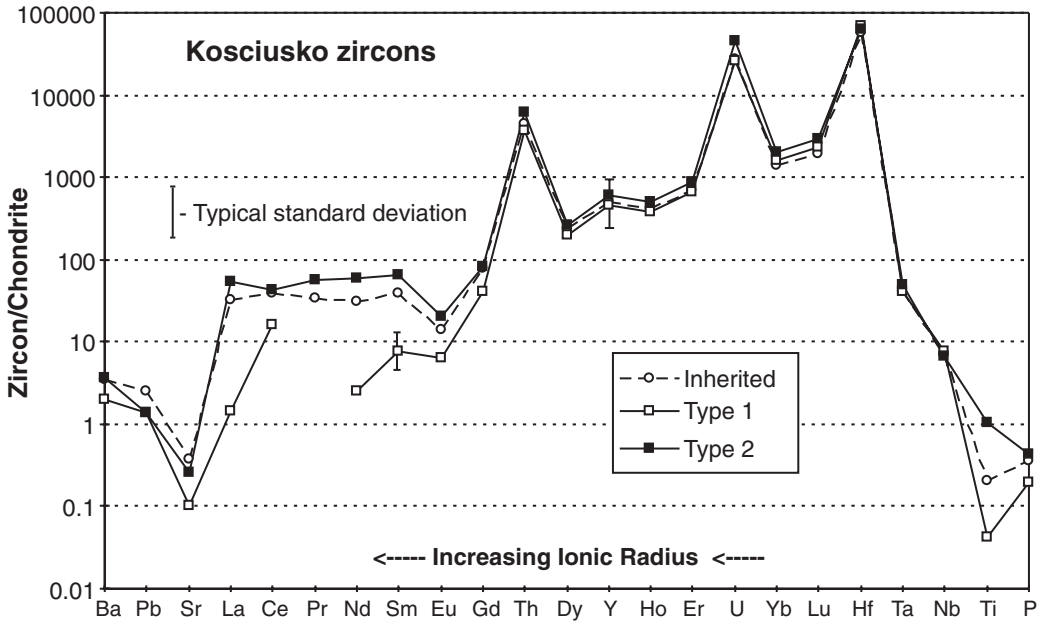

Fig. 10. Trace element patterns of zircon populations from the Kosciusko tonalite. Data are from Table 1.

There is clear evidence of type 1 zircon overgrown by type 2 (Fig. 8a), where type 1 is often partly resorbed. In contrast, there is very gradual transition in crystal morphology from type 2 to type 3 zircon (Fig. 8c).

Zircon trace element composition

Kosciusko tonalite

The averaged trace element data for the zircon populations are given in Table 1. Trace element data obtained for zircon grains of type 1 show a depletion in the light rare earth elements (LREE; Fig. 10), in contrast to the trace element pattern of type 2, which is comparatively enriched in LREE and has a more pronounced Eu anomaly but a smaller Ce anomaly. These data imply that there was a change in host magma composition from zircon type 1 to type 2. Inherited zircons show trace element patterns close to those of type 2 zircon, suggesting that the composition of the source rocks was similar to that of the magma from which type 2 zircon grains crystallized.

Berridale adamellite

The trace element pattern of the type 1 zircon population is very distinctive, having higher Mn and lower La, Ta and P concentrations, and a very weak Eu anomaly, compared with other groups (Table 2; Fig. 11a). To emphasize the contrasts in trace element composition among the zircon populations from the Berridale adamellite, the trace element content of each type has been normalized to type 1 (Fig. 11b).

The trace element compositions of the type 2 zircon are distinguished by high U, Ba, Sr and LREE contents compared with the other zircon types (Fig. 11). Europium shows a pronounced negative anomaly, suggesting that abundant feldspar crystallization took place during or before the crystallization of this type of zircon.

The trace element analyses of type 3 zircon grains show very low concentrations of Ba, Sr, Mn and LREE, commonly below the level of detection. Type 3 also has the weakest Eu anomalies and relatively high Pb, Nb and heavy REE (HREE) contents. The main geochemical features of group 4 zircons are relatively low Pb, Sr, Ba, Th, Mn and middle REE (MREE) contents in comparison with the other populations (Fig. 11, Table 2).

The distinct trace element patterns found in the different types of zircon, and especially the large variations in LREE abundances and size of the Eu anomaly, suggest definite changes in the composition of the magmas from which these different types crystallized. The inherited zircon in the Berridale sample also shows a distinctive trace element pattern with significantly lower U, Th and LREE contents and a weak Eu anomaly, suggesting that this grain was derived from a different magma source.

Dundee rhyodacite ignimbrite

Trace element data show that zircon grains of type 1 have higher HREE abundances than the other two groups, but the LREE abundances are intermediate compared with other two types (Fig. 12; Table 3). Ba, Sr, Nb, Mn and Ga are below the detection limit. Type 2 zircons are characterized by high LREE, Sr, Ti and P contents. The trace

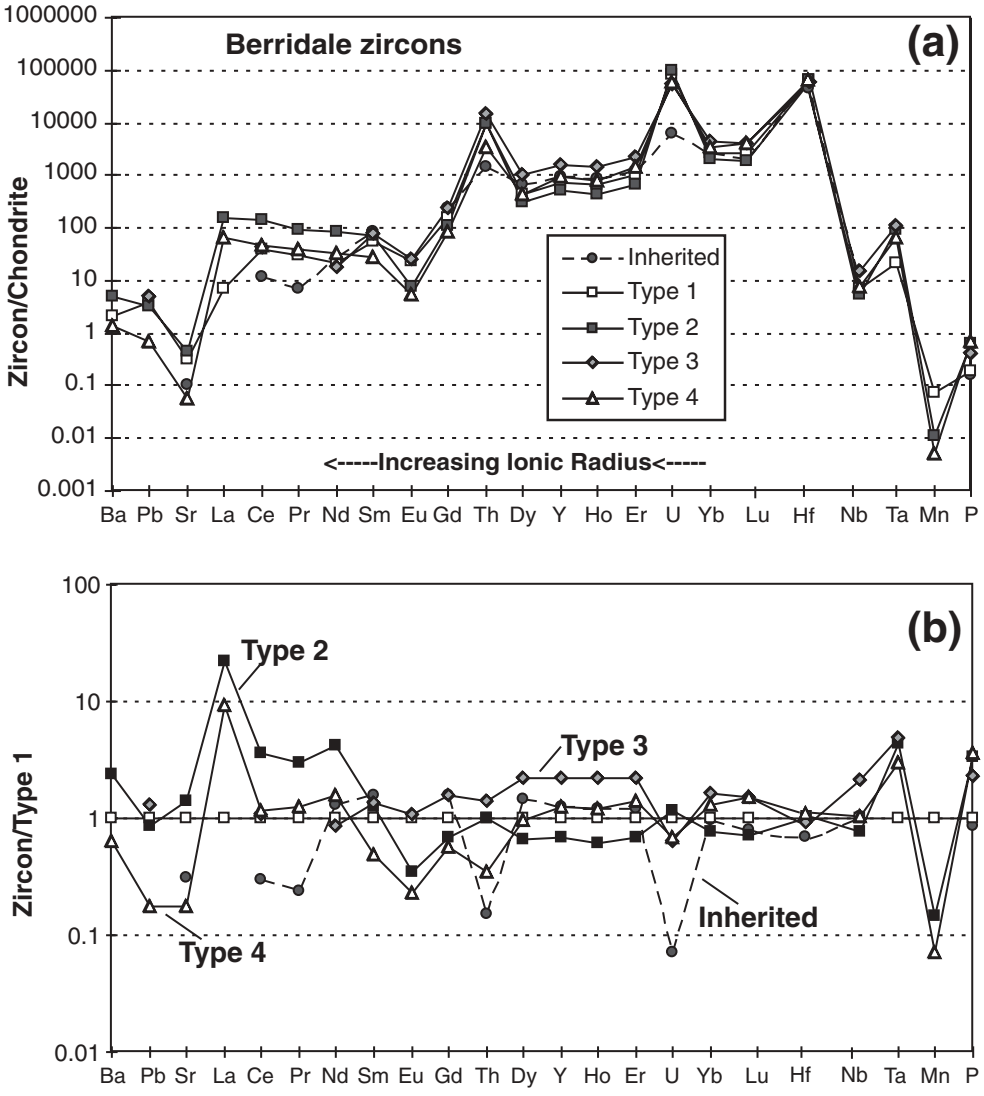

Fig. 11. Average trace element patterns of zircon populations from the Berridale adamellite. (a) Chondrite-normalized patterns; (b) zircon types normalized to Type 1.

element pattern of the type 3 zircon population is well defined, having a positive Ce anomaly and a more pronounced negative Eu anomaly than the other groups as well as relatively low Sr, Ti, P and MREE.

Zircon U–Pb ages

Kosciusko tonalite

Eleven zircon grains (13 analyses) have been used for the U–Pb age determination (Fig. 13; Table 1). Most of the grains from this sample give similar ages and only four analyses were rejected for the further age calculation. Core and rim data for grain 6 were rejected because of the presence of a large common-Pb component (the $^{208}Pb/^{232}Th$ age is much older than $^{206}Pb/^{238}U$ age). The analysis of the core of grain 3 was also disregarded because of apparent Pb loss; grain 7 gave an age much older than the rest of the population (489 ± 13 Ma; Fig. 13a) and is interpreted as inherited. The remaining nine grains give a $^{206}Pb/^{238}U$ age of 418 ± 4 Ma (MSWD = 0·63; Fig. 13b); this is accepted as the best estimate of the crystallization age of this sample.

Berridale adamellite

U–Pb dating was performed on eight grains (13 analyses) from this sample (Table 2). Grain 5, which was recognized as inherited because of its distinct internal and external morphology, yielded the oldest age of 1090 ± 28 Ma. Cores of zircons 3 and 9, described as morphological type 1, produced ages of 508 ± 13 Ma and 461 ± 12 Ma, respectively, which are noticeably older than ages

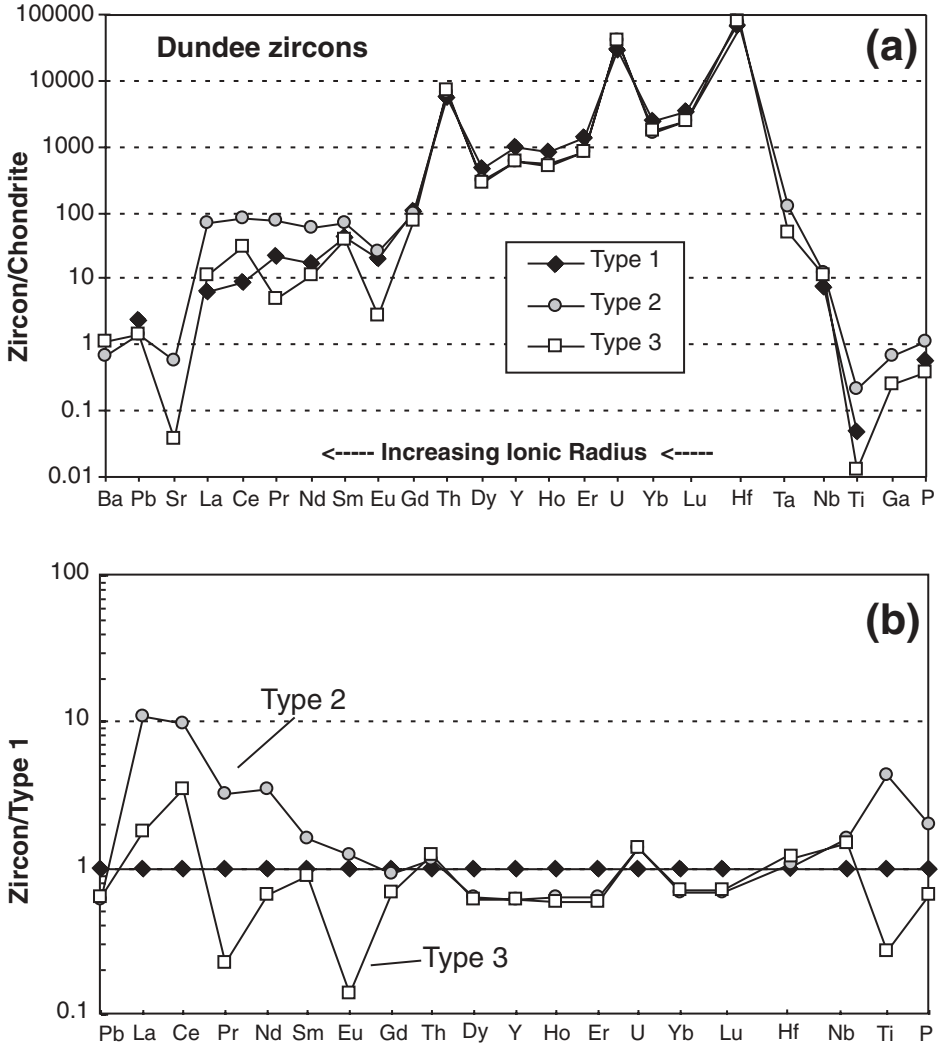

Fig. 12. Average trace element patterns of zircon populations from the Dundee rhyodacite ignimbrite. (a) Chondrite-normalized patterns; (b) zircon types normalized to Type 1.

found in other types. These two grains also show the lowest $^{176}Hf/^{177}Hf$ ratios in the sample (see below). Another two points (3-rim1 and 4-rim) were rejected from the age calculation because their age reflects a mixture of zircon core and rim as shown in Fig. 14a. A regression through the remaining six grains gives a crystallization age for this rock of 435 ± 5 Ma (Fig. 14b).

Dundee rhyodacite ignimbrite

Seven zircon grains (11 points) have been dated from the Dundee rhyodacite ignimbrite (Fig. 15a; Table 3). Apart from four points (analyses 1 core, 4 core, 1 rim and 6 rim), which were rejected because of high common-Pb contents, all other analyses are identical within the analytical uncertainty and give a weighted mean age of 257·6 ± 2·5 Ma (MSWD = 0·70, probability = 0·65; Fig. 15b).

Zircon Hf isotope signatures

Kosciusko tonalite

There is very little variation in Hf isotopic composition between type 1 and 2 zircon from the Kosciusko tonalite (Fig. 16). The $^{176}Hf/^{177}Hf$ ratio ranges from 0·28240 to 0·28247 for type 2 and the average (0·28243 ± 0·00003) is identical within error to that of the type 1 zircons (0·28242 ± 0·00003; Table 1; Fig 16). ε_{Hf} values range from −1·3 to almost −4 and T_{DM} ages give a minimum age for the source material of about 1·10–1·16 Ga. The crustal model ages (T_{DM}^{C}) range from 1·25 to 1·60 Ga. However, some cores in zircon grains from the Kosciusko tonalite show much more radiogenic Hf isotope signatures with $^{176}Hf/^{177}Hf$ as high as 0·28258 and $\varepsilon_{Hf} = 2·02$ (grain 3; Table 1), whereas other core analyses show values very similar to those found in rims.

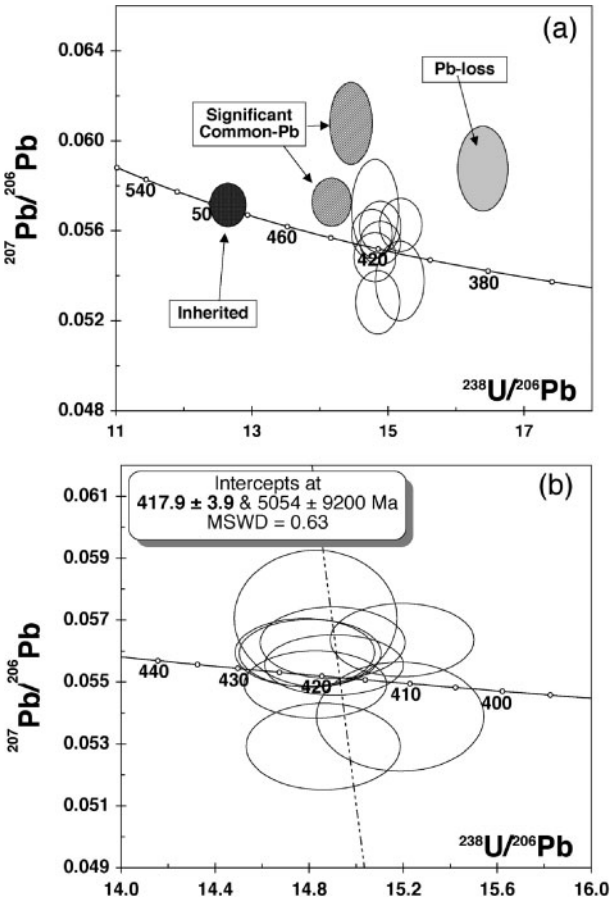

Fig. 13. Tera–Wasserburg (or 'inverse concordia') plot for zircon grains from the Kosciusko tonalite: (a) all data, $n = 13$; (b) only analyses used for the age calculation, $n = 9$, MSWD = 0·63.

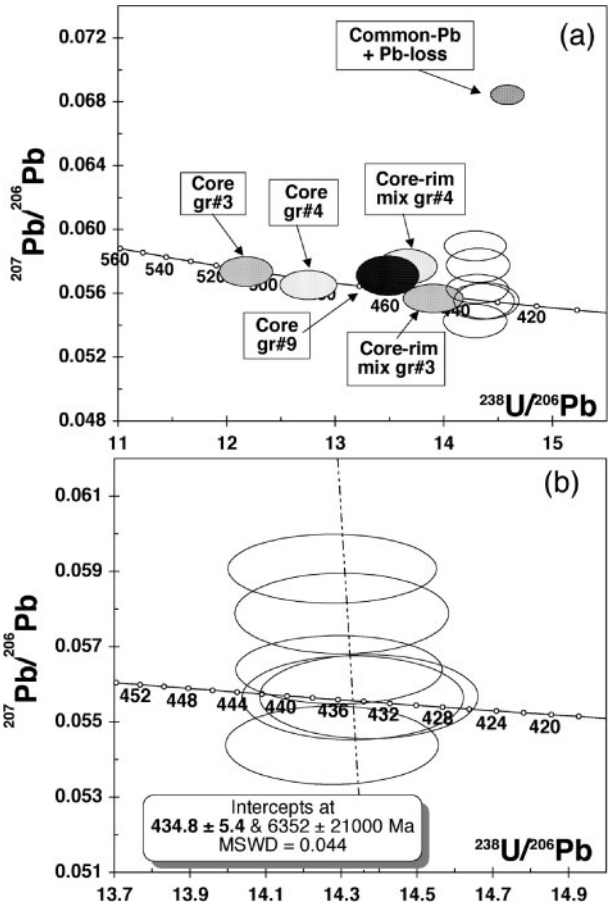

Fig. 14. Tera–Wasserburg plot for zircon grains from the Berridale adamellite: (a) all data apart from the oldest inherited grain 5, $n = 12$; (b) only analyses used for the age calculation, $n = 6$, MSWD = 0·044.

Berridale adamellite

In contrast to the Kosciusko tonalite, zircon from the Berridale adamellite shows an appreciable variation in its Hf isotope composition. The lowest $^{176}Hf/^{177}Hf$ ratios are found in type 1 zircon, with average values of 0·28225 ± 0·00002 (Table 2; Fig. 17) and crustal model ages of 1·90–1·98 Ga (T_{DM}^{C}). The highest Hf isotope ratios, up to 0·282432, are typical of zircon types 3 and 4. These types also show a wider range of ε_{Hf} (from about −3 to −9) and model ages (T_{DM} varies from 1·2 to 1·4 Ga and T_{DM}^{C} from 1·56 to 1·87 Ga). The inherited grain 5 shows a very distinct Hf isotope composition with a much higher $^{176}Hf/^{177}Hf$ ratio (0·28255 ± 0·00002; $\varepsilon_{Hf} = 1.59$; Table 2) compared with those seen in other zircon types from the same sample.

Dundee rhyodacite ignimbrite

The most distinguishing feature of zircon from the Dundee rhyodacite ignimbrite is its radiogenic Hf isotope ratios and positive ε_{Hf} values (4·7–8·8; Table 3), about 5–10 ε_{Hf} units higher than the values seen in the zircon populations from the S-type granitoids. The estimated minimum model age (T_{DM}) of the source material ranges from 530 to 700 Ma and the crustal model age is around 700–950 Ma.

Despite the general complexity in the Hf isotope signatures and large variations in $^{176}Hf/^{177}Hf$ ratios even within a single morphological type, there are several core–rim overgrowths indicating significant changes in the Hf isotope composition, which correlate well with the recognized changes in grain morphology (Fig. 18). For example, the core of grain 4, described as type 1, has $^{176}Hf/^{177}Hf = 0.28282 \pm 0.00002$; it is overgrown by a type 2 rim with $^{176}Hf/^{177}Hf = 0.28277 \pm 0.00002$, a difference that is well outside the analytical uncertainly. Furthermore, the core of grain 3 represents morphological type 2 and has $^{176}Hf/^{177}Hf = 0.28275 \pm 0.00002$, whereas in the grain's rim, described as type 3, $^{176}Hf/^{177}Hf = 0.28283 \pm 0.00002$. However, there is much less variation in the core–rim pairs within a single zircon type (Fig. 18).

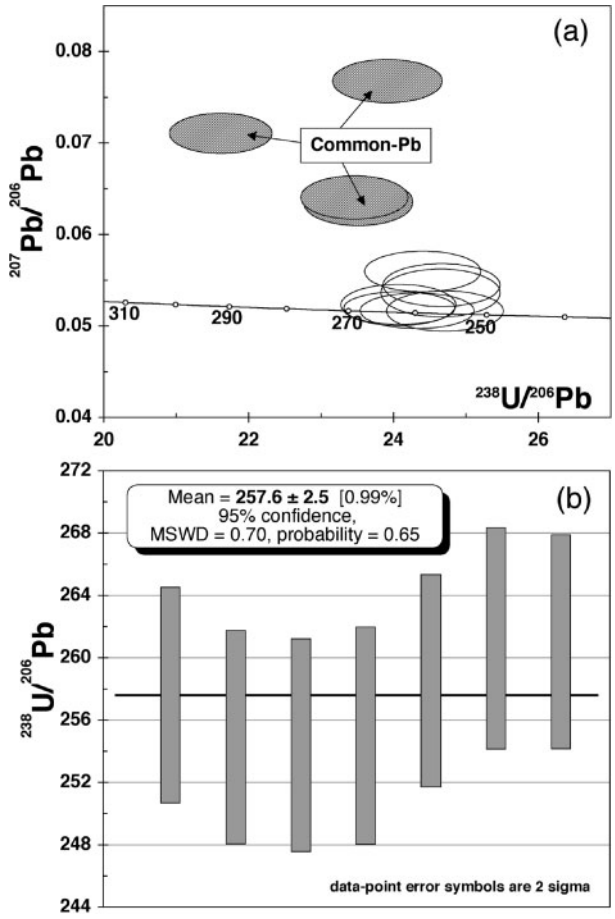

Fig. 15. (a) Tera–Wasserburg plot for zircon grains from the Dundee rhyodacite ignimbrite, all data ($n = 11$); (b) weighted average diagram with weighted mean age of 257·6 ± 2·5 Ma, $n = 6$, MSWD = 0·70, probability = 0·65.

DISCUSSION

Zircon from the Kosciusko tonalite

The gradual change in morphology of the Kosciusko zircon suggests that zircon was crystallizing as the magma cooled and became more alkaline (Fig. 5); there is no morphological evidence to suggest abrupt changes in magma composition. The trace element patterns show gradual enrichment in the LREE, a decrease in the Ce anomaly and deepening of the negative Eu anomaly from type 1 to type 2 (Fig. 10). These changes are consistent with simple fractional crystallization during magma cooling, as the evolving liquid becomes enriched in incompatible elements and feldspar crystallization leads to enhancement of the negative Eu anomaly. Some overgrowths of type 2 zircon by type 1 and again by type 2 zircon (Fig. 4a) could reflect temperature fluctuations, perhaps related to magma movements.

The morphological and trace element signatures of the Kosciusko zircon grains indicate that they originated from geochemically similar sources of crustal origin (Fig. 3). This is also supported by the homogeneous Hf isotopic composition and identical U–Pb age found in zircons from this sample. All of the isotopic and trace element data thus are consistent with the crystallization and/or fractionation of a single magma during a general decrease in temperature, as originally suggested by the evolution in zircon morphology. Low $^{176}Hf/^{177}Hf$ ratios and negative ε_{Hf} values indicate the involvement of of crustally-derived components in the production of this tonalite (Fig. 19); Hf model ages suggest that the source materials were at least 600 Myr older than the magma-generation event. This is consistent with the definition of the tonalite as S-type. There is no evidence of magma mixing in this particular sample and the whole process is consistent with control by fractional crystallization during cooling.

Zircon from the Berridale adamellite

Zircon grains from the Berridale adamellite have complex internal morphology (Fig. 6), which reflects changes in both the temperature and the composition of the magma and provides a qualitative record of magma evolution (Fig. 7). Evidence of overgrowth of type 1 zircon by type 2 (Fig. 6a and c) shows the direction of magma evolution. The patterns suggest that zircon was crystallizing as the magma cooled and became more alkaline; the late-stage heating and compositional change (types 3 and 4) imply a mixing between the original magma and a new, hotter batch. U–Pb data distinguish age populations (Fig. 14), including some inherited grains seen as zircon cores in the BSE–CL images (Fig. 6), and confirm that the recognized morphological types 1–4 crystallized over a relatively short time span. The trace element patterns of the zircon characterize the original magma types and trace their evolution (Fig. 11). Thus from type 1 to type 2, the magma became enriched in LREE and depleted in HREE, and developed a negative Eu anomaly, consistent with the crystallization of plagioclase and mafic minerals. Type 3 shows a reversal of this trend, consistent with the introduction of a new batch of magma, which then evolved toward type 4 with further crystallization of plagioclase. The Hf isotope data allow an evaluation of the relative contribution of mantle-derived and crustal-derived components in the production of the host granitoids (Fig. 17), and help track the mixing of magmas with different sources. The rise in $^{176}Hf/^{177}Hf$ between type 2 and type 3 requires a new magma batch, and shows that it was derived from a more primitive (mantle-like, or 'I-type') source than the original magma that precipitated the type 1–2 zircons. The zircon 'tape-recorders' thus show that the S-type Berridale adamellite had at least two distinct sources, including a significant I-type magma contribution.

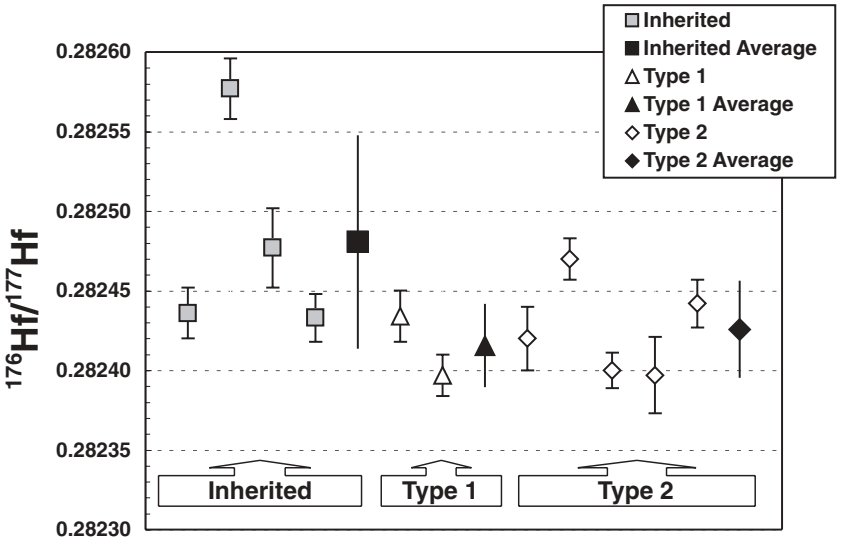

Fig. 16. $^{176}Hf/^{177}Hf$ ratios in zircon populations from the Kosciusko tonalite: open symbols represent single analyses; filled symbols averaged data for the type.

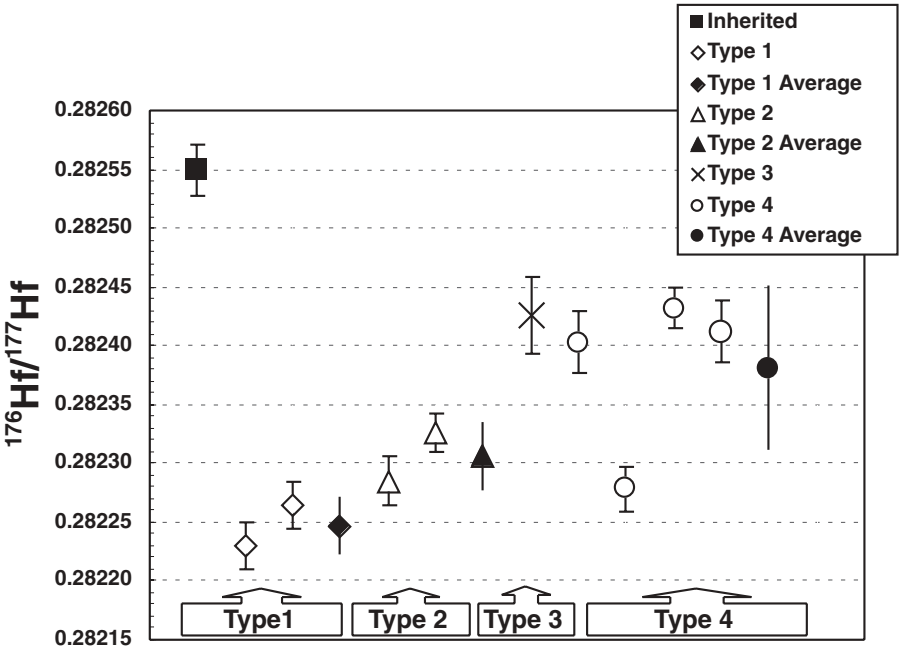

Fig. 17. $^{176}Hf/^{177}Hf$ ratios in zircon populations from the Berridale adamellite: open symbols represent single analyses; filled symbols averaged data for the type.

However, there is a major disagreement between the Hf isotopic data and the morphological classification in this case. According to Pupin's scheme (Fig. 7), type 1 and type 2 zircon (particularly type 1) have crystal growth forms typical of zircons in mantle-derived melts, but these two types have the lowest ε_{Hf} values, indicating a crustal origin for the host magma (Fig. 19). Types 3 and 4, in turn, show crystal forms typical of zircon from crustal-derived magmas, but their Hf isotopes are more radiogenic (i.e. more juvenile) than the other types.

It is important to note here that the inherited zircon grains commonly found in the S-type granitoids are also recognized in the Berridale adamellite. One inherited grain (grain 5; Table 2) has characteristics typical of zircon derived from juvenile sources, such as

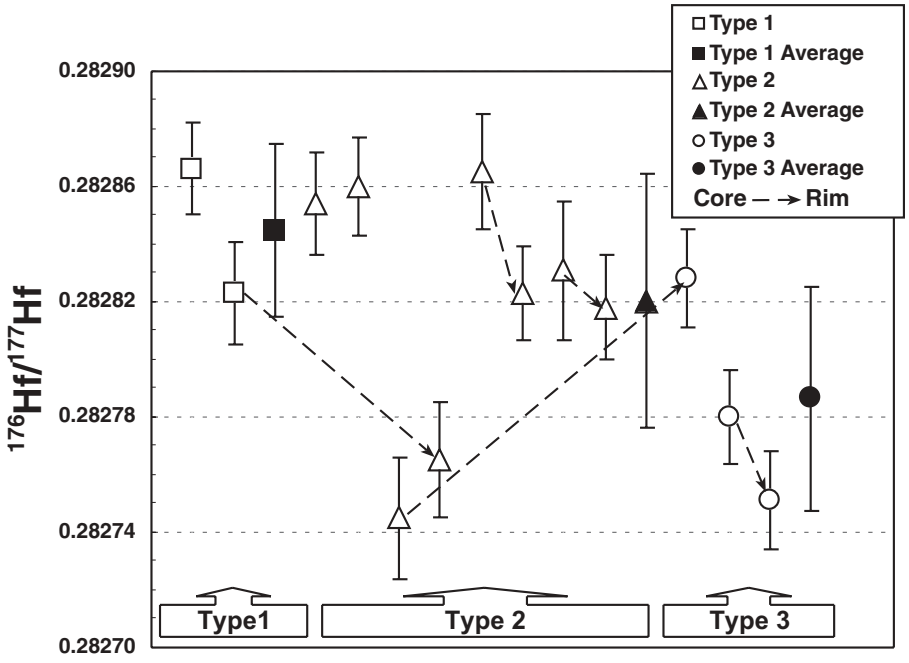

Fig. 18. $^{176}Hf/^{177}Hf$ ratios in zircon populations from the Dundee rhyodacite ignimbrite; open symbols represent single analysis; filled symbols averaged data for the type. Dashed lines connect core and rim of the same grains.

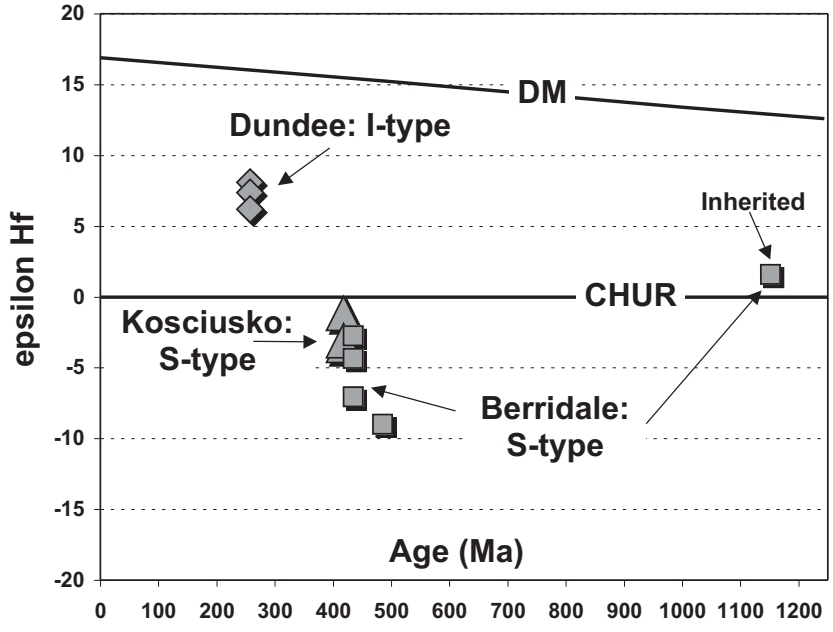

Fig. 19. Averaged ε_{Hf} data for each zircon morphological type plotted against its U–Pb age, where the DM line represents Depleted Mantle and CHUR is the Chondritic Unfractionated Reservoir.

unfractionated trace element patterns, high $^{176}Hf/^{177}Hf$ ratio and positive ε_{Hf} values. This observation implies the presence of I-type sources.

There are several possible scenarios of magma evolution for the Berridale adamellite: (1) there was an evolution from type 1 to type 4 liquids, interrupted by the input of a new liquid (type 3 magma) of different, relatively mafic composition and higher temperature; or (2) there were two independent sources, which evolved along two fractionation trends, the first represented by zircons of types 1 and 2, and the second by types 3 and 4, before finally being mixed to form the analysed rock; or,

finally, (3) types 1–2, 3 and 4 represent three distinct components that combined in the composite magma chamber (Fig. 11). The last suggestion is consistent with Collins' (1996) three-component mixing model, in which the Lachlan Fold Belt S-type magmas are heavily contaminated by I-type magmas. According to this model, the Berridale adamellite is the product of mixing between magmas with juvenile signatures (possibly very young underplated magmas), partially melted older mafic lower crust and partially melted supracrustal rocks in the middle crust. In this case, zircon of types 1–2 could be products of mantle-derived magmas, type 3 represents the partially melted lower crust and type 4 is derived from supracrustal rocks of the middle crust. This assumption is consistent with the crystal morphology of the recognized populations, but is difficult to reconcile with the Hf isotopic data.

Taking into consideration the remarkable differences in Hf isotope signatures recorded in zircon types 1–2 and 3–4, and the lack of evidence for overgrowth of type 2 by types 3 or 4, the second scenario with two independent sources is regarded as the most probable model of magma evolution for the Berridale adamellite. This model, based on zircon morphological and isotopic evidence, agrees with Collins' (1996) suggestion that there was a significant contribution of I-type magmas during the generation of this S-type granitoid.

Zircon from the Dundee rhyodacite ignimbrite

The evolution of zircon morphology in the Dundee rhyodacite (Figs 3 and 9) shows that although the parental granitic magma is mainly of mantle origin according to Pupin's scheme, the presence of partly resorbed type 1 zircon typical of S-type granitoids implies the involvement of crustal material in the source magma. Morphologically, type 1 zircon grains found in the Dundee rhyodacite ignimbrite are very similar to the type 2 zircon of the S-type Kosciusko tonalite.

The trace element pattern of each zircon type from the Dundee rhyodacite ignimbrite shows its own, quite distinct REE features (Fig. 12): type 1 crystallized from a relatively 'primitive' magma with low LREE and a weak Eu anomaly; type 2 has a strong enrichment of the LREE; type 3 shows the depletion of MREE and the deepest Eu anomaly. The type 3 pattern could develop from type 2 by the fractionation of accessory minerals that concentrate LREE and MREE (e.g. apatite, titanite, allanite), and abundant crystallization of plagioclase.

Generally high $^{176}Hf/^{177}Hf$ ratios, positive ε_{Hf} values, and a scarcity of inherited zircon in this sample emphasize the distinct characteristics typical of I-type granitoids (Fig. 19). However, the evidence of complex morphology together with variations in Hf isotope composition (core–rim relationships in particular) indicate there was a moderate contribution of crustal material to the source magma. The partial melting of crustal material is recorded by the dissolution features in some zircon grains; further magmatic overgrowths are controlled by a simple fractional crystallization trend represented by the grain morphology typical for I-type magmas.

CONCLUSIONS

This study of zircon populations using an integrated approach relating morphology, trace element composition and Hf isotope composition can provide important additional data to constrain models of granitoid petrogenesis. This approach provides a sensitive test for the involvement of both mantle-derived and crustal-derived components in the production of granitoids. The sampled rock is the result of mixing of these components and the zircon uniquely records the processes involved (Griffin *et al.*, 2002). This type of information is rarely obtainable by studies of bulk-rock compositions or the common magmatic minerals.

The examples presented here show that changes in zircon morphology, as described in the classification developed by Pupin (1980) generally correlate with changes in trace element and Hf isotope signatures, defining the mixing of magma sources and the direction of magma evolution. In most cases, zircons from S-type granitoids show various combinations of forms with a prominent presence of {211} pyramids, and those from the I-type magmas tend to have {101} pyramids as their dominant form. The crustal or mantle derivation of specific magma types predicted by Pupin's (1980) scheme is, in some cases, not consistent with the Hf isotope data. However, the combination of crystal morphology, trace element patterns and Hf isotope data provides a robust approach for studying the generation of granitoid magmas.

ACKNOWLEDGEMENTS

We are grateful to Bruce Chappell for generously providing samples of granitoids from eastern Australia and information on those samples. We also thank Tom Bradley for sample preparation, and Norm Pearson, Ashwini Sharma and Suzy Elhlou for their constant assistance with analytical work. Constructive comments by Stirling Shaw led to improvements of this manuscript and are very much appreciated. The manuscript was also improved by reviews from G. Clarke and an anonymous referee. Funding for this work was provided by a scholarship from CRAE, an Australian Postgraduate Award, an ARC Discovery grant (E.A.B.) and an

Australian Research Council Large grant (S.Y.O'R. and W.L.G.). This is Publication 406 from the ARC National Key Centre for Geochemical Evolution and Metallogeny of Continents (www.es.mq.edu.au/GEMOC/).

REFERENCES

Bea, F. (1996). Controls on the trace element composition of crustal melts. *Transactions of the Royal Society of Edinburgh: Earth Sciences* **87**, 33–41.

Belousova, E. A., Walters, S., Griffin, W. L., O'Reilly, S. Y. & Fisher, N. I. (2002). Zircon trace-element compositions as indicators of source rock type. *Contributions to Mineralogy and Petrology* **143**, 602–622.

Berezhnaya, N. G. (1999). Criteria for the genetic typification of zircon from metamagmatic associations of the Aldan Shield. *Doklady Earth Sciences* **368**(7), 982–984. (Translated from *Doklady Akademii Nauk* **368**(3), 373–375.)

Bizzarro, M., Baker, J. A., Haack, H., Ulfbeck, D. & Rosing, M. (2003). Early history of Earth's crust–mantle system inferred from hafnium isotopes in chondrites. *Nature* **421**, 931–933.

Black, L. P. & Gulson, B. L. (1978). The Age of the Mud Tank carbonatite, Strangways Range, Northern Territory. *BMR Journal of Australian Geology and Geophysics* **3**, 227–232.

Blichert-Toft, J., Chauvel, C. & Albarède, F. (1997). The Lu–Hf geochemistry of chondrites and the evolution of the mantle–crust system. *Earth and Planetary Science Letters* **148**, 243–258.

Chappell, B. W. (1996). Magma mixing and the production of compositional variation within granite suites: evidence from the granites of southeastern Australia. *Journal of Petrology* **37**, 449–470.

Chappell, B. W. & White, A. J. R. (1974). Two contrasting granite types. *Pacific Geology* **8**, 173–174.

Chappell, B. W. & White, A. J. R. (1992). I- and S-type granites in the Lachlan Fold Belt. *Transactions of the Royal Society of Edinburgh: Earth Science* **83**, 1–26.

Chappell, B. W., White, A. J. R. & Wyborn, D. (1987). The importance of residual source material (restite) in granite petrogenesis. *Journal of Petrology* **28**, 1111–1138.

Cherniak, D. J., Hanchar, J. M. & Watson, E. B. (1997*a*). Diffusion of tetravalent cations in zircon. *Contributions to Mineralogy and Petrology* **127**, 383–390.

Cherniak, D. J., Hanchar, J. M. & Watson, E. B. (1997*b*). Rare-earth diffusion in zircon. *Chemical Geology* **134**, 289–301.

Clarke, D. B. (1992). *Granitoid Rocks*. London: Charman & Hall, 283 pp.

Collins, W. J. (1996). Lachlan Fold Belt granitoids: products of three-component mixing. *Transactions of the Royal Society of Edinburgh: Earth Sciences* **87**, 171–181.

Corfu, F., Hanchar, J. M., Hoskin, P. W. O. & Kinny, P. (2003). Atlas of zircon textures. In: Hanchar, J. M. & Hoskin, P. W. O. (eds) *Zircon. Reviews in Mineralogy and Geochemistry* **53**, 469–499.

Fowler, A., Prokoph, A. & Dupuis, C. (2002). Organization of oscillatory zoning in zircon: analysis, scaling, geochemistry, and model of a zircon from Kipawa, Quebec, Canada. *Geochimica et Cosmochimica Acta* **66**, 311–328.

Gray, C. M. (1984). An isotopic mixing model for the origin of granitic rocks in southeastern Australia. *Earth and Planetary Science Letters* **70**, 47–60.

Gray, C. M. (1990). A strontium isotopic traverse across the granitic rocks of southeastern Australia: petrogenetic and tectonic implications. *Australian Journal of Earth Sciences* **37**, 331–349.

Griffin, W. L., Pearson, N. J., Belousova, E. A., Jackson, S. R., van Achterbergh, E., O'Reilly, S. Y. & Shee, S. R. (2000). The Hf isotope composition of cratonic mantle: LAM-MC-ICPMS analysis of zircon megacrysts in kimberlites. *Geochimica et Cosmochimica Acta* **64**, 133–147.

Griffin, W. L., Wang, X., Jackson, S. E., Pearson, N. J., O'Reilly, S. Y., Xu, X. & Zhou, X. (2002). Zircon chemistry and magma genesis, SE China: *in-situ* analysis of Hf isotopes, Pingtan and Tonglu igneous complexes. *Lithos* **61**, 237–269.

Griffin, W. L., Belousova, E. A., Shee, S. R., Pearson, N. J. & O'Reilly, S. Y. (2004). Archean crustal evolution in the northern Yilgarn Craton: U–Pb and Hf-isotope evidence from detrital zircons. *Precambrian Research* **131**, 231–282.

Heaman, L. M., Bowins, R. & Crocket, J. (1990). The chemical composition of igneous zircon suites: implications for geochemical tracer studies. *Geochimica et Cosmochimica Acta* **54**, 1597–1607.

Hoskin, P. W. O. & Schaltegger, U. (2003) The composition of zircon and igneous and metamorphic petrogenesis. In: Hanchar, J. M. & Hoskin, P.W.O. (eds) *Zircon. Reviews in Mineralogy and Geochemistry* **53**, 27–62.

Jackson, S. E., Pearson, N. J., Griffin, W. L. & Belousova, E. A. (2004). The application of laser ablation microprobe-inductively coupled plasma-mass spectrometry (LAM-ICP-MS) to *in situ* U–Pb zircon geochronology. *Chemical Geology* **211**, 47–69.

Krasnobayev, A. A. (1986). *Zircon as an Indicator of Geological Processes* (in Russian), Moscow: Nauka, 146 pp.

Leitch, E. C., Iwasaki, M., Watanabe, T., Iizumi, S., Ishiga, H. & Kawachi, Y. (1988). The structure of the southern part of the New England Fold Belt. *Preliminary Report on the Geology of the New England Fold Belt, Australia* **1**, 9–31.

Murali, A. V., Parthasarathy, R., Mahadevan, T. M. & Sankar Das, M. (1983). Trace element characteristics, REE patterns and partition coefficients of zircons from different geological environments—a case study on Indian zircons. *Geochimica et Cosmochimica Acta* **47**, 2047–2052.

Nagasawa, H. (1970). Rare earth concentrations in zircon and apatite and their host dacites and granites. *Earth and Planetary Science Letters* **9**, 359–364.

Norman, M. D., Pearson, N. J., Sharma, A. & Griffin, W. L. (1996). Quantitative analysis of trace elements in geological materials by laser ablation ICPMS: instrumental operating conditions and calibration values of NIST glasses. *Geostandards Newsletter* **20**(2), 247–261.

Norman, M. D., Griffin, W. L., Pearson, N. J., Garcia, M. O. & O'Reilly, S. Y. (1998). Quantitative analysis of trace element abundances in glasses and minerals: a comparison of laser ablation ICPMS, solution ICPMS, proton microprobe, and electron microprobe data. *Journal of Analytical Atomic Spectroscopy* **13**, 477–482.

Pupin, J. P. (1980). Zircon and granite petrology. *Contributions to Mineralogy and Petrology* **73**, 207–220.

Scherer, E., Munker, C. & Mezger, K. (2001). Calibration of the lutetium–hafnium clock. *Science* **293**, 683–687.

Shaw, S. E. & Flood, R. H. (1981). The New England Batholith, eastern Australia: geochemical variations in time and space. *Journal of Geophysical Research* **86**, 10530–10544.

Soesoo, A. (2000). Fractional crystallization of mantle-derived melts as a mechanism for some I-type granite petrogenesis: an example from Lachlan Fold Belt, Australia. *Journal of the Geological Society, London* **157**, 135–149.

Taylor, S. R. & McLennan, S. M. (1985). *The Continental Crust: its Composition and Evolution*. Oxford: Blackwell Scientific, 312 pp.

Varva, G. (1993). A guide to quantitative morphology of accessory zircon. *Chemical Geology* **110**, 15–28.

Vervoort, J. D. & Blichert-Toft, J. (1999). Evolution of the depleted mantle: Hf isotope evidence from juvenile rocks through time. *Geochimica et Cosmochimica Acta* **63**, 533–556.

Wang, X. (1998). Quantitative description of zircon morphology and its dynamics analysis. *Science in China, Series D* **41**(4), 422–428.

Wang, X. & Kienast, J. R. (1999). Morphology and geochemistry of zircon: a case study on zircon from the microgranitoid enclaves. *Science in China, Series D* **42**, 544–552.

Watson, E. B. (1979). Zircon saturation in felsic liquids: experimental results and applications to trace element geochemistry. *Contributions to Mineralogy and Petrology* **70**, 407–419.

Watson, E. B. (1996). Dissolution, growth and survival of zircons during crustal fusion: kinetic principles, geological models and implications for isotopic inheritance. *Transactions of the Royal Society of Edinburgh: Earth Sciences* **87**, 43–56.

Watson, E. B. & Cherniak, D. J. (1997). Oxygen diffusion in zircon. *Earth and Planetary Science Letters* **148**, 527–544.

Watson, E. B. & Harrison, T. M. (1983). Zircon saturation revisited: temperature and compositional effects in a variety of crustal magma types. *Earth and Planetary Science Letters* **64**, 295–304.

White, A. J. R. & Chappell, B. W. (1977). Ultrametamorphism and granitoid genesis. *Tectonophysics* **43**, 7–22.

Wiedenbeck, M., Alle, P., Corfu, F., Griffin, W. L., Meier, M., Oberli, F., Von Quart, A., Roddick, J. C. & Spiegel, W. (1995). Three natural zircon standards for U–Th–Ph, Lu–Th, trace element and REE analyses. *Geostandards Newsletter* **19**(1), 1–23.